Characterization and correction of serial deferred charge in LSST camera ITL CCDs

Adam Snyder,[a,*] **Emily Longley**,[b] **Craig Lage**,[a] **Seth Digel**,[c,d] **Homer Neal**,[c,d] **Yousuke Utsumi**,[c,d] **and Aaron Roodman**[c,d]

[a]University of California, Davis, Department of Physics, Davis, California, United States
[b]Duke University, Department of Physics, Durham, North Carolina, United States
[c]Stanford University, Kavli Institute for Particle Astrophysics and Cosmology, Stanford, California, United States
[d]SLAC National Accelerator Laboratory, Menlo Park, California, United States

Abstract. Electro-optical testing and characterization of the Vera C. Rubin Observatory Legacy Survey of Space and Time Camera has shown that the focal plane charge-coupled devices developed by Imaging Technology Laboratory exhibit serial deferred charge signal in excess of the expected proportional deferred charge loss from global charge transfer inefficiency. We model the additional deferred charge as resulting from localized charge trapping in the serial register and from a signal-dependent electronic offset effect. A physically motivated forward deferred charge simulation algorithm and a reverse deferred charge correction algorithm were developed in order to correct for deferred charge during data reduction and reduce the possible impacts on Rubin Observatory project science goals. We apply the correction algorithm to calibration data and demonstrate the ability to reduce deferred charge signal measured in the overscan pixel regions and remove the serial pixel correlations resulting from the redistribution of charge between pixel neighbors during readout. © *2021 Society of Photo-Optical Instrumentation Engineers (SPIE)* [DOI: 10.1117/1.JATIS.7.4.048002]

Keywords: charge-coupled devices; sensors; Vera C. Rubin Observatory; Legacy Survey of Space and Time.

Paper 21054 received May 5, 2021; accepted for publication Sep. 27, 2021; published online Oct. 15, 2021.

1 Introduction

The Vera C. Rubin Observatory, currently under construction at Cerro Pachón in Chile, will perform an unprecedented wide, fast, and deep survey of the southern sky using the 3.2-gigapixel Legacy Survey of Space and Time (LSST) camera, the largest digital camera ever constructed. The science goals of the Rubin Observatory Project are to probe the nature of dark matter and dark energy, take an inventory of the solar system, explore the transient sky, and to map the Milky Way.[1] The heavily segmented focal plane consists of 189 fully depleted silicon charge-coupled devices (CCDs) arranged into 21 science raft tower modules (RTMs) that contain all the necessary mechanical, thermal, and electronic support components. Four specialized corner raft tower modules (CRTMs) are also included in the focal plane to be used for wavefront sensing and guiding capabilities. Individual CCDs are further subdivided into 16 segments, each of which has its own independent serial register and output amplifier, in order to perform a full-frame readout in ∼2 s.

Integration and testing of the LSST camera focal plane is currently being performed at the SLAC National Accelerator Laboratory. Each RTM first undergoes metrology and electro-optical testing using a single-raft cryostat, referred to as Test Stand 7 (TS7), in conjunction with a separate test bench named Test Stand 8 (TS8).[2] Following this raft-level testing period, the RTMs are stored safely to await installation into the LSST camera focal plane. Assembly, focal plane metrology, and electro-optical characterization of the RTMs following integration into the

*Address all correspondence to Adam Snyder, aksnyder@ucdavis.edu

2329-4124/2021/$28.00 © 2021 SPIE

Downloaded From: https://www.spiedigitallibrary.org/journals/Journal-of-Astronomical-Telescopes,-Instruments,-and-Systems on 03 Oct 2023
Terms of Use: https://www.spiedigitallibrary.org/terms-of-use

LSST camera are performed using the bench for optical testing (BOT). The BOT consists of a large dark box, support systems for installation of the LSST camera cryostat, and an XY-motor-platform stage used for the mounting of optical test equipment. A detailed description of the BOT requirements, design, and the supporting test equipment is provided by Newbry et al.[3] The integration and testing first proceeds with a period of partial focal plane testing, where only a subset of RTMs are installed, in order to perform preliminary testing of the hardware and software subsystems used to control the operation of the LSST camera cryostat, prior to full focal plane operation.

Throughout each testing period, the LSST camera CCDs undergo electro-optical characterization and optimization to ensure conformity with the project sensor requirements and to identify any sensor effects that may impact the final science goals. An important area of research is the characterization of instrument signatures introduced during the readout of the CCD pixel arrays. The transfer of charge (electrons for the case of LSST camera CCDs) from pixel-to-pixel via voltage clocking during readout will not be a completely efficient process. Charge carriers that are not transferred are referred to as deferred charge and will result in spurious trails of signal following bright pixels that can impact astronomical source astrometry and shape measurements.[4,5] The deferred charge of a CCD can be characterized as the charge transfer inefficiency (CTI), defined by the amount of charge that has not been transferred between two pixels, divided by the charge in the first pixel before the transfer. Charge transfer is mediated by the mechanisms of self-induced drift, fringing field drift, and thermal drift that will theoretically set the level of CTI and the deferred charge that occurs at each pixel transfer.[6] The total amount of deferred charge is also increased by the presence of charge traps within the pixel array that redistribute charge between pixels by means of capture and release during readout. Readout electronics effects, in particular those that involve the sense node reset and the electronic offset, may also introduce tails of spurious signal that will resemble the effect of deferred charge but do not involve the physical transfer of charge from one pixel to another.[7]

During both the raft-level testing and partial focal plane testing of the LSST camera, it was found that a large number of the segments of CCDs manufactured by Imaging Technology Laboratories (ITL), model number STA3800C, had CTI measurements that were larger than expected. These results indicated that there were additional deferred charge contributions that could introduce systematic errors into the Rubin Observatory project analyses and that necessitated the development of a new correction algorithm to be applied during data reduction. In Sec. 2, we first present the results of the detailed characterization of the observed deferred charge effects and the determination of the various sources of deferred charge in ITL CCDs. A discussion of the impact of the deferred charge on the serial correlation calculations used for the determination of the brighter-fatter correction kernel is presented in Sec. 3. Section 4 details a new simulated model of the readout process, developed to recreate the observed deferred charge. An algorithm to reverse the readout model and correct the deferred charge is described in Sec. 5. The procedure to derive the deferred charge correction parameters for each CCD segment is outlined in Sec. 6. Finally, testing and validation of the deferred charge correction applied to existing flat-field data is presented in Sec. 7.

2 Deferred Charge Characterization

The data used in this study were taken during a period of partial focal plane operation as part of the integration and testing period of the LSST camera. During this time, nine science-grade RTMs (a total of 81 CCDs) and the four CRTMs were installed into the focal plane, the Camera Cryostat was placed under vacuum, and the sensors were cryogenically cooled to an operating temperature of −100°C. Of the nine science-grade RTMs installed, four RTMs were composed of ITL STA3800C CCDs, whereas the remaining five RTMs consisted of CCDs manufactured by Teledyne e2v (Fig. 1).

This study will focus on serial deferred charge effects measured for ITL CCDs (Fig. 2); there have been no comparable effects measured for either parallel pixel transfer or in Teledyne e2v CCDs. Detailed results for a single CCD, R02/S02 (named by raft slot and sensor slot) are shown throughout this paper as an illustrative example, but the majority of the ITL CCDs that will be

Downloaded From: https://www.spiedigitallibrary.org/journals/Journal-of-Astronomical-Telescopes,-Instruments,-and-Systems on 03 Oct 2023
Terms of Use: https://www.spiedigitallibrary.org/terms-of-use

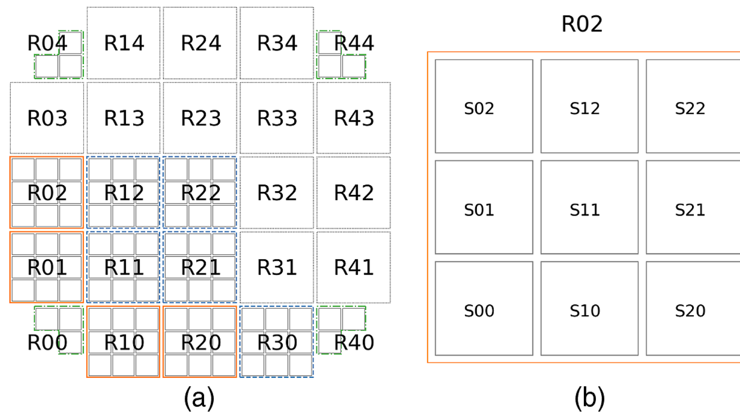

Fig. 1 (a) Diagram of LSST camera focal plane during the nine-raft testing period, showing ITL RTMs (orange solid outline), Teledyne e2v RTMs (blue dashed outline), corner RTMs (green dash-dotted outline), and uninstalled RTMs (black dotted outlines) labeled by raft slot names. (b) Diagram of a single RTM showing nine CCDs labeled by sensor slot names.

Table 1 Operating voltage values for LSST ITL 3800C CCDs during the partial focal plane testing period.

Voltage name	Set value (V)
Output gate	–2.0
Reset drain	13.0
Output drain	25.0
Reset gate high	8.0
Reset gate low	–2.0
Serial clock high	5.0
Serial clock low	–5.0
Parallel clock high	2.0
Parallel clock low	–8.0
Backside bias	–50.0

used in the final focal plane configuration show similar behavior. A more general summary of serial CTI measurements for the population of ITL CCDs tested during the partial focal plane testing period is provided in Fig. 6.

The ITL CCDs in the focal plane are all operated using the same set of voltages, summarized in Table 1. Full-frame readout is synchronized across all science sensors and is performed in 2 s, corresponding to 2 ms per single-pixel readout, which informs the pixel transfer time.

2.1 *EPER Analysis*

One method for calculating the CTI from a flat-field image with signal S_{FF} is the extended pixel edge response (EPER) method[6] expressed as

$$\mathrm{CTI}(\mathrm{S}_{\mathrm{FF}}) = \frac{S_O}{N_T S_{\mathrm{LP}}}, \tag{1}$$

where the CTI ratio is estimated by calculating the ratio of the signal in the overscan pixels S_O compared to the signal of the last physical pixel S_{LP} (not necessarily equal to S_{FF}), including a

Downloaded From: https://www.spiedigitallibrary.org/journals/Journal-of-Astronomical-Telescopes,-Instruments,-and-Systems on 03 Oct 2023
Terms of Use: https://www.spiedigitallibrary.org/terms-of-use

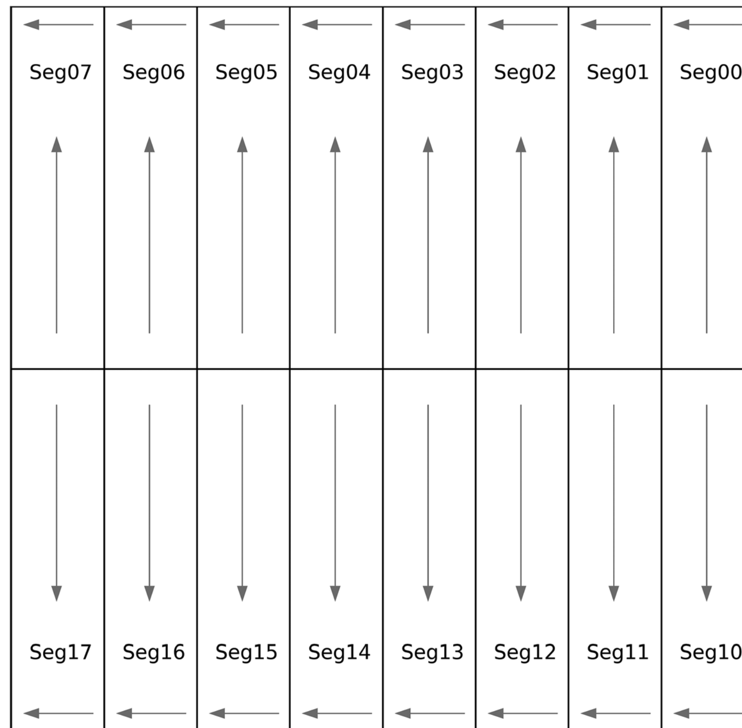

Fig. 2 LSST camera ITL STA3800C CCD segment layout with segment name labels. Arrows indicate the direction of parallel and serial transfer during readout.

factor of N_T representing the number of pixel transfers needed to readout the pixel array up to the overscan region. This equation results from the binomial approximation of the accumulation of deferred charge occurring at every pixel transfer; as such, this value is a good representation of the deferred charge behavior only when the inefficiency is caused by a proportional amount of charge loss at each pixel transfer. This category of deferred charge, referred to as global CTI, is most commonly associated with the charge transfer mechanisms for each pixel transfer and the presence of bulk traps or radiation-induced traps distributed uniformly throughout the bulk silicon.[6] It is important to note that the amount of signal measured in the overscan pixels may also include contributions from "localized" charge trapping that break the EPER method assumption of dependence on the number of pixel transfers N_T.

The desired level for serial CTI in LSST camera CCDs is $<5 \times 10^{-6}$, calculated using the EPER method applied to flat-field images taken at signals of 1000 electrons and 50,000 electrons. To produce a more detailed characterization of the deferred charge behaviors for the LSST camera CCDs, we evaluated the serial CTI using flat-field images drawn from a data set consisting of more than 200 pairs of flat-field images taken at illumination signal levels logarithmically spaced from 100 electrons to above 150,000 electrons, where blooming full well effects become dominant.

The flat-field illumination was provided by a custom optical projector, using a commercial near-IR enhanced Zeiss 25 mm 2.8/f wide-angle lens to reimage the exit port of an integrating sphere across the full camera focal plane. The illumination light, provided by a Quartz Tungsten Halogen Lamp, was passed through a Sloan Digital Sky Survey i color filter manufactured by Astrodon, resulting in a bandpass spanning wavelengths between roughly 700 and 850 nm.

All flat-field images were calibrated using gain values measured from 55Fe soft x-ray measurements and the images were corrected for electronic bias and offset. Electronic offset correction was performed row-by-row, using the mean value of the serial overscan pixels (64 serial overscan pixels per row). The first 5 and last 2 serial overscan pixels were omitted from the mean value calculation in order to reduce the contributions from deferred charge in the first several overscan pixels and large noise in the final overscan pixels, which was historically observed in earlier single-sensor testing. Electronic bias correction was performed using an electronic offset

Downloaded From: https://www.spiedigitallibrary.org/journals/Journal-of-Astronomical-Telescopes,-Instruments,-and-Systems on 03 Oct 2023
Terms of Use: https://www.spiedigitallibrary.org/terms-of-use

corrected superbias image, in order to remove any additional electronic spatial non-uniformity in the images.

The serial CTI calculations using the EPER method were made using the sum of the signal in the first two serial overscan pixels to represent S_O. Because each row of the segment image is exposed to the same serial register and readout behavior, the photon shot noise and read noise (<7 electrons) can be greatly suppressed by taking the mean over the CTI results for each of the individual 2000 rows in the pixel array. The results of the CTI from EPER as a function of flat-field signal level for CCD R02/S02 are shown in Fig. 3. The range of deferred charge behavior is striking. In addition to elevated serial CTI at low signal levels in a subset of segments, almost all segments show large jumps in serial CTI at signal levels between 10,000 electrons and 100,000 electrons, well below signal levels where blooming full well effects would be observed. The rapid fluctuations of CTI below 1000 electrons are caused by the serial overscan pixel signal becoming subdominant to the read noise.

A more comprehensive representation of the overscan behavior for all segments of sensor R02/S02 is provided by Fig. 4. The mean signal measured in the first 15 serial overscan pixels, as a function of flat-field signal, is plotted using a color mapping that is linear between −1 and 1, and logarithmic elsewhere, in order to display the overscan pixel behavior over a wide range of values. All 16 segments exhibit elevated signal extending into overscan pixels up to 15 pixels beyond the last physical pixel. This effect is strongest for flat-field signals approaching blooming

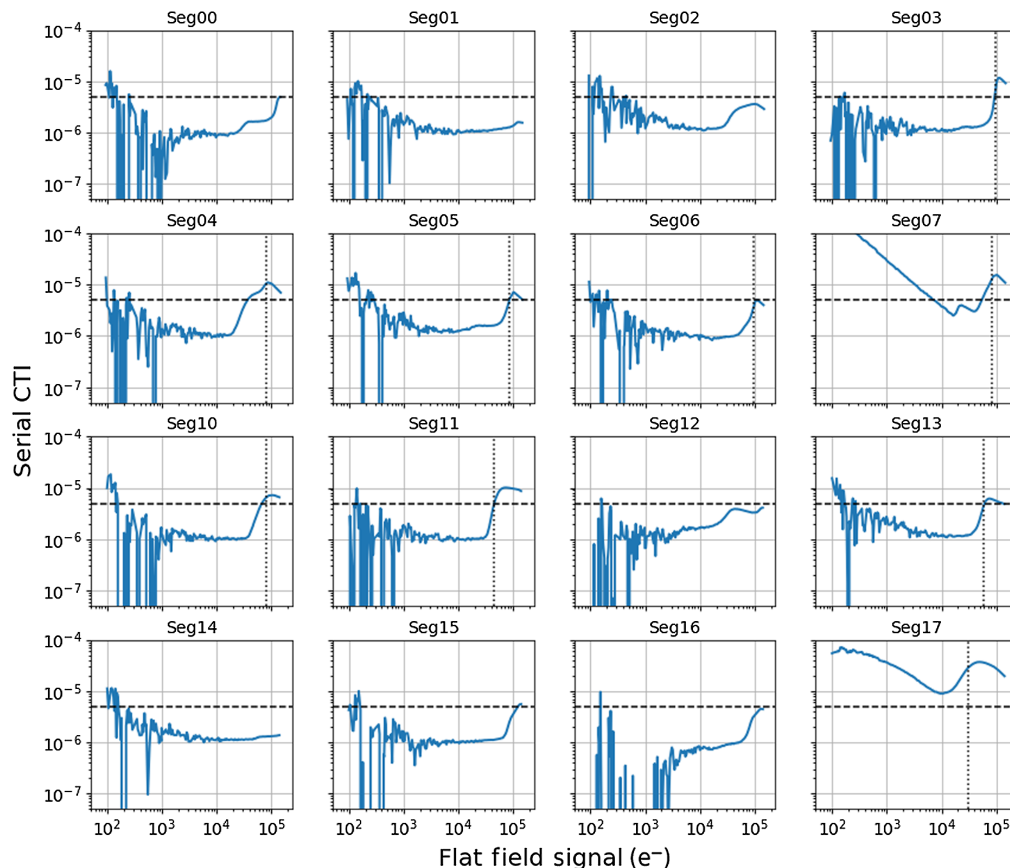

Fig. 3 Serial CTI calculated using the EPER method for the 16 segments of a single ITL STA3800C CCD. Here the sum of the signal in the first two serial overscan pixels was used as the numerator in the CTI ratio equation. Many segments exhibit large and varying levels of CTI across the range of signal levels; below flat-field signals of 10^3 electrons the serial overscan pixel signal becomes subdominant to the read noise. The horizontal dashed line represents the desired maximum serial CTI value of 5×10^{-6}. The vertical dotted lines plotted in a set of subplots indicate per-segment signal levels of interest and are reproduced at the same flat-field signal value across Figs. 3, 5, 7, 12, 14, and 18.

Downloaded From: https://www.spiedigitallibrary.org/journals/Journal-of-Astronomical-Telescopes,-Instruments,-and-Systems on 03 Oct 2023
Terms of Use: https://www.spiedigitallibrary.org/terms-of-use

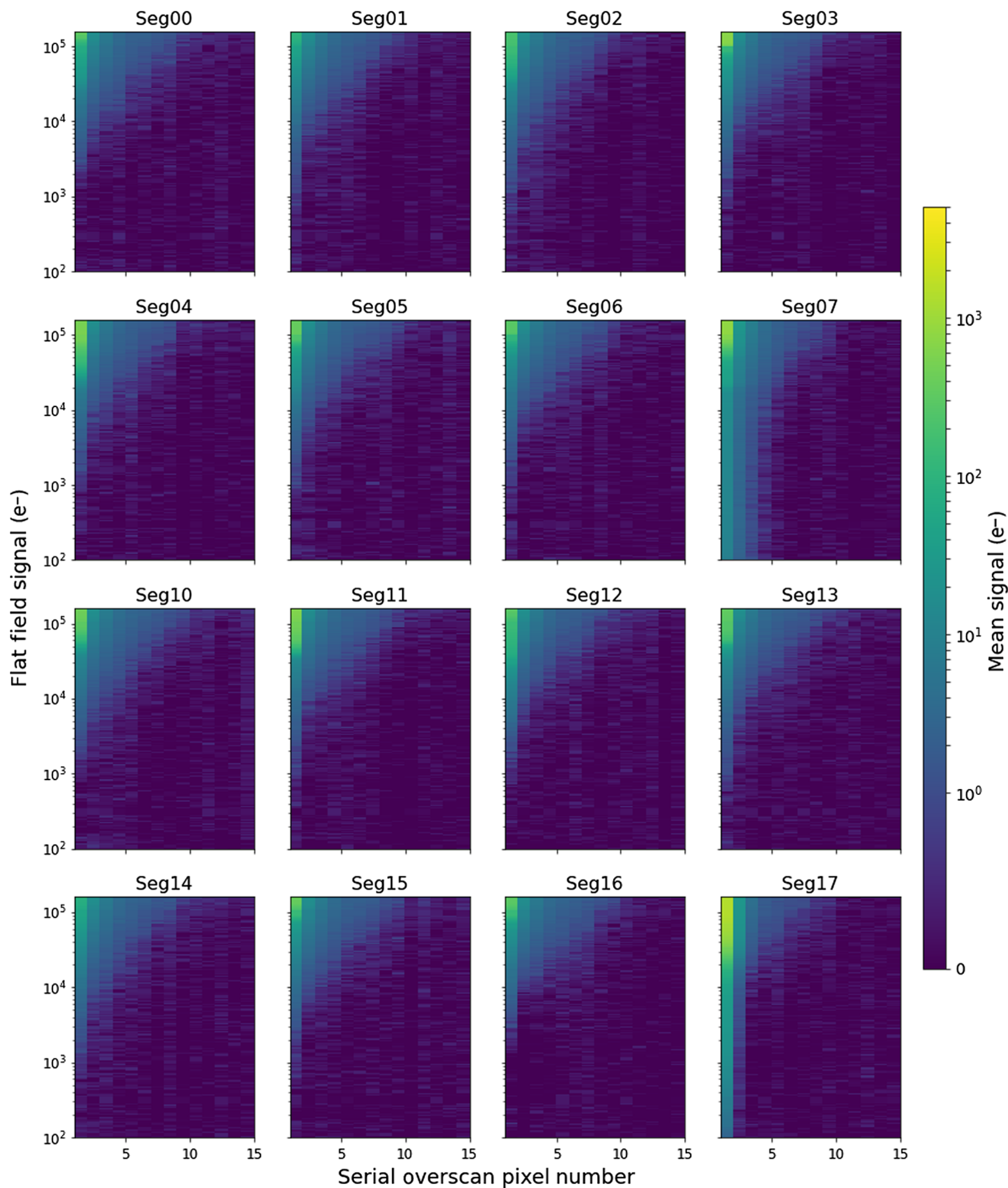

Fig. 4 Mean signal in serial overscan pixels after a flat-field image (displayed on a symmetric log color scale with linear cutoff of 1.0 electron) for flat-field signal levels from 100 to 150,000 electrons, for each CCD segment. Error on the mean signal is 0.14 electrons. As the signal of the flat-field increases (*y* axis of each subplot), the deferred charge signal (color scale) increases and extends further into the serial overscan pixels (*x* axis of each subplot).

full well values and is roughly equal in magnitude and in rate of decay across all segments, although Seg07 and Seg17 are visible outliers in this regard.

Figure 5 shows a plot of the mean signal in the first three overscan pixels of each segment, each as a function of flat-field signal. A subset of segments (e.g., Seg01 and Seg14) show roughly linear increase of the signal in the first overscan pixel, consistent with CTI loss that is proportional to the pixel signal. However, the remainder exhibit non-linear behavior in the measured signal of the first serial overscan pixel that directly corresponds to the observed large jumps in serial CTI in each of these segments. With the exception of Seg07 and Seg17, all segments show a linear increase of the signal in the second and third overscan pixel, regardless of any non-linear behavior of the first overscan pixel signal. This behavior can be explained by deferred charge signal from two components: a slowly decaying linear component that extends

Downloaded From: https://www.spiedigitallibrary.org/journals/Journal-of-Astronomical-Telescopes,-Instruments,-and-Systems on 03 Oct 2023
Terms of Use: https://www.spiedigitallibrary.org/terms-of-use

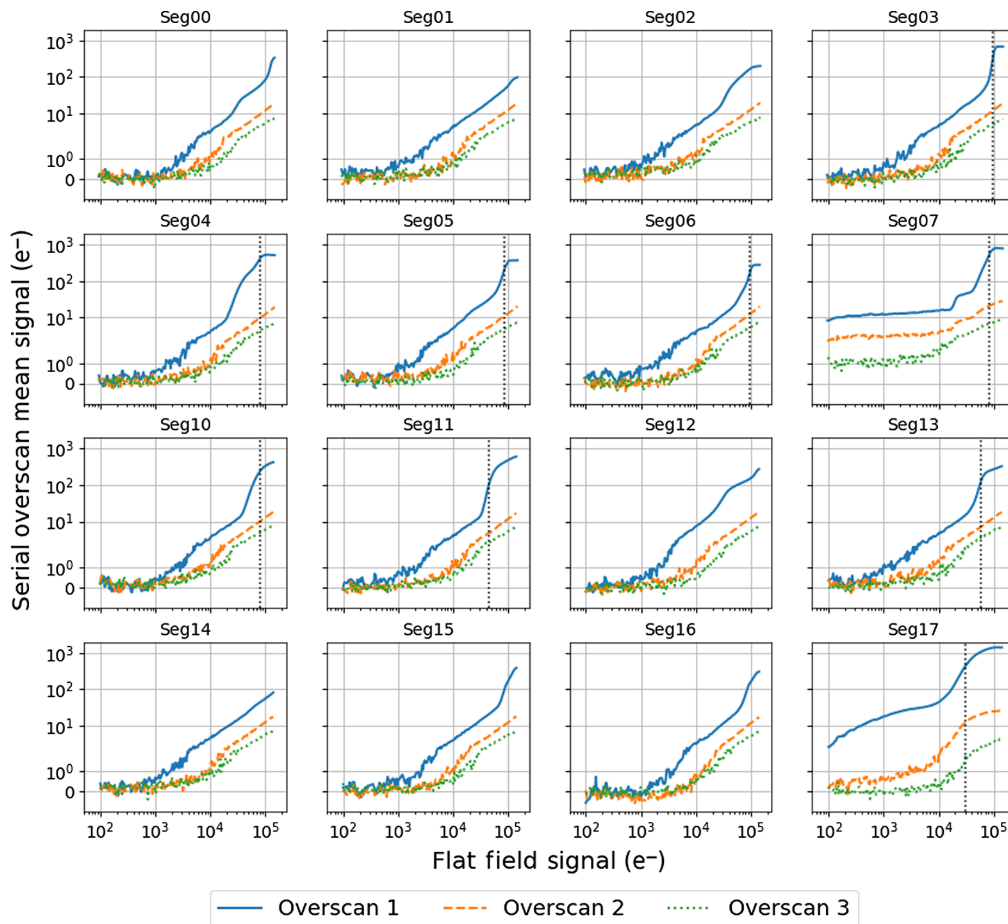

Fig. 5 Mean signal in each of the first three serial overscan pixels for all 16 segments of a single ITL 3800C CCD. Many segments exhibit large jumps in the mean signal in the first overscan pixel. Error on the mean overscan pixel signals is 0.14 electrons. The vertical dotted lines plotted in a set of subplots indicate per-segment signal levels of interest and are reproduced at the same flat-field signal value across Figs. 3, 5, 7, 12, 14, and 18.

beyond the first three overscan pixels and a rapidly decaying non-linear component that primarily affects only the first overscan pixel.

To summarize the deferred charge behavior, there are two separate effects that are observed. The first is that a subset of segments show non-linear increases in serial CTI calculated from EPER and in pixel signal in the first serial overscan pixel. The second is that all segments show exponential decaying tails roughly proportional to the last pixel signal extending many pixels into the serial overscan. The LSST camera CCDs are manufactured from high-quality silicon and are not radiation damaged; therefore there should only be an extremely limited quantity of single-electron traps distributed throughout the bulk silicon that could contribute to increased deferred charge. The deferred charge signal measured in the serial overscan pixels is expected to be predominately caused by the global CTI set by the charge transfer mechanisms, resulting in deferred charge at every pixel transfer that is roughly linear with pixel signal. In contrast, the serial CTI measurements show evidence for serial deferred charge from additional effects. A more detailed description of the determination of these additional sources of deferred charge is provided by Snyder and Roodman.[8] Here we summarize the conclusions of deferred charge resulting from a combination of charge trapping and electronic effects, as well as provide new measurements in support of these conclusions.

The first observed deferred charge behavior, the large jumps in the measured serial CTI observed in Fig. 3 and in the first serial overscan pixel in Fig. 5, can be caused by a variable amount of deferred charge within the serial register due to a localized charge trap, i.e., charge

Downloaded From: https://www.spiedigitallibrary.org/journals/Journal-of-Astronomical-Telescopes,-Instruments,-and-Systems on 03 Oct 2023
Terms of Use: https://www.spiedigitallibrary.org/terms-of-use

trapping occurring at a single-pixel location. In order to accommodate multiple output amplifiers per CCD, the serial registers of each of the 16 segments contain additional prescan pixels that bend away from the pixel array; the constricted region where the buried channel navigates this bend is the likely location of a spurious potential pocket, the size of which is heavily dependent on the specific electrostatic conditions in this region that can act as a localized charge trap. Measurements of the dependence of 55Fe soft x-ray profile widths on position in the pixel array have provided the strongest evidence that the large jumps in serial CTI are not caused by poor global CTI, but instead by a localized effect that is independent on the number of pixel transfers.[8] New measurements of serial covariances (Sec. 3) also support this model of charge trapping by a potential pocket in the serial prescan pixels. The extent of this trapping appears to be greatly variable from segment to segment, though there is evidence that segments whose output amplifiers are positioned near the sensor edge (Seg07 and Seg17) are most affected.

Due to the absence of significant populations of bulk or radiation-induced traps and considering that measurements of parallel CTI are routinely on the order of 10^{-7}, the second observed deferred charge behavior, the presence of exponentially decaying tails of signal above the read noise in pixels extending far into the overscan region in all segments, is better modeled as an electronic coupling between the sense node or output amplifier and the bulk silicon, rather than bulk charge trapping that occurs only within the serial register but not in the imaging region in the parallel direction.[8] In this model, the electronic offset will have a "local" component that is proportional to the signal of pixels that have previously been read out and that decays at an approximately exponential rate, producing tails of signal in the overscan regions that resemble deferred charge tails (Fig. 4). This behavior was also noted in the previous studies of the ITL serial deferred charge using a single sensor, where it was determined that the characteristic decay time for the exponential decay of the tail was between 5 and 3 μs (roughly 2.5 and 1.5 serial pixel

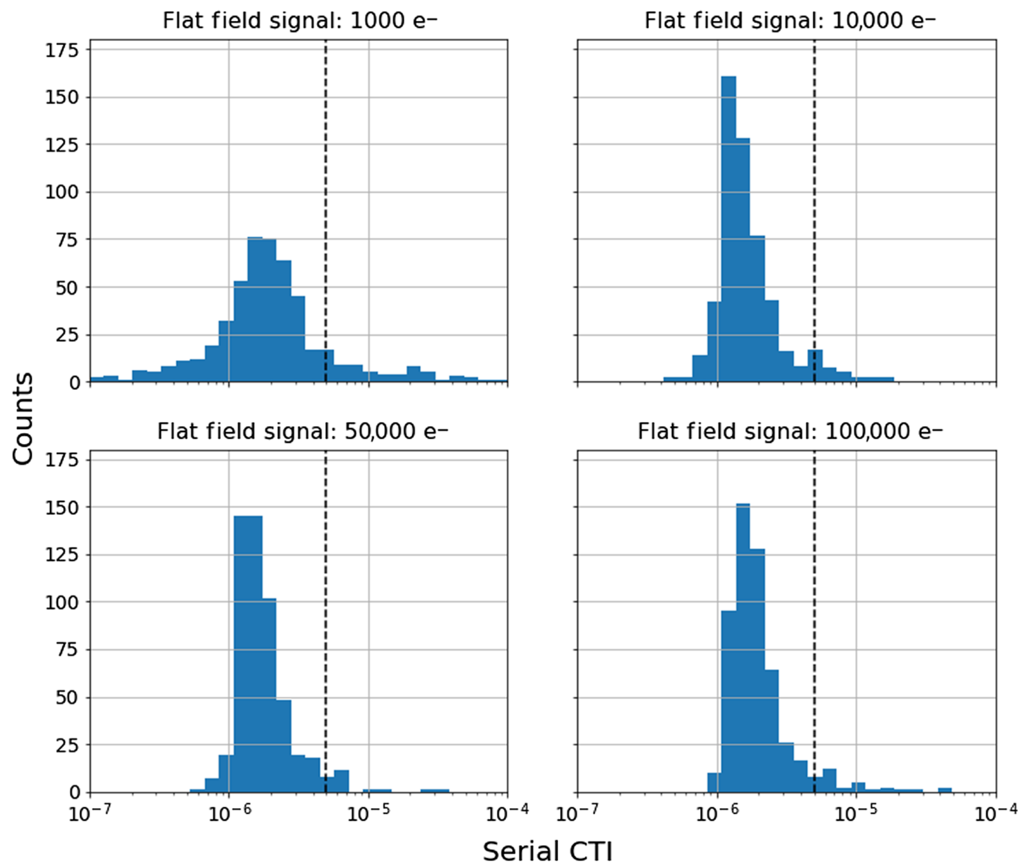

Fig. 6 Histogram of serial CTI values for all ITL CCD segments during the partial focal plane testing period measured using the EPER method from flat-field images taken at four different signal levels. The vertical dashed line represents the desired maximum serial CTI value of 5×10^{-6}.

Downloaded From: https://www.spiedigitallibrary.org/journals/Journal-of-Astronomical-Telescopes,-Instruments,-and-Systems on 03 Oct 2023
Terms of Use: https://www.spiedigitallibrary.org/terms-of-use

transfers), which is inconsistent with the characteristic release times for known single-electron traps at $-100°C$ in silicon.[8] As a characteristic of the output amplifier or sense node, it is expected that astronomical sources in the imaging pixel region would also be susceptible to the same tails of signal. This has not yet been confirmed during focal plane testing using images of projected realistically sized sources, however, a number of future studies intend to attempt to measure this effect.

Figure 6 shows the distribution of effective serial CTI values calculated using the EPER method for all segments of the ITL CCD sensors installed in the Camera Cryostat during the period of partial focal plane testing at four different flat-field signal levels. Although the majority of ITL CCD segments have measured serial CTI below the desired level of 5×10^{-6}, the distributions are skewed toward higher values of serial CTI in each of the four cases shown. ITL CCD R02/S02, which was used to generate the more detailed graphs of overscan signal behavior, has a number of segment examples with high measured serial CTI contributing to the skew of the distribution. These include Seg07 and Seg17 at low flat-field signals, whereas the majority of the segments on ITL CCD R02/S02 are examples at high flat-field signals. The number of segments with higher values of serial CTI and the variation in their behavior is sufficient enough to require a deferred charge correction to be included in the image data reduction process.

3 Serial Pixel Covariances

Redistribution of charge due to any charge trapping will result in not only spurious charge signal tails but will also cause neighboring pixels to become increasingly correlated, as seen in measurements of the pixel covariances. A pixel signal $s_{m,n}$ that is affected by serial deferred charge will be modified by an amount $\epsilon_{m,n}$ representing charge lost from the original pixel signal to traps and an amount $\epsilon_{m,n-1}$ representing charge captured from the preceding pixel (in the serial direction) that has been released from traps:

$$s'_{m,n} = s_{m,n} + \epsilon_{m,n-1} - \epsilon_{m,n}. \tag{2}$$

From this expression, in terms of the expectation value of the redistributed charge $E[\epsilon_{m,n}]$ caused by deferred charge, the changes in the covariance

$$\mathrm{cov}[s'_{m,n}, s'_{m,n-1}] = \mathrm{cov}[s_{m,n}, s_{m,n-1}] + \mathrm{var}[s'_{m,n}] \frac{dE[\varepsilon_{m,n}]}{ds_{m,n}} \tag{3}$$

and changes in the variance

$$\mathrm{var}[s'_{m,n}] = \mathrm{var}[s_{m,n}] \left(1 - 2\frac{dE[\varepsilon_{m,n}]}{ds_{m,n}}\right) \tag{4}$$

can be calculated, as outlined by Astier et al.[9] Both the covariance and variance will have a component that is dependent on the derivative of the expectation value of the redistributed charge $E[\epsilon_{m,n}]$ caused by deferred charge. This relationship allows for a method to study the deferred charge behavior using pixel data from the imaging region; in contrast, the analyses presented in Sec. 2 relied on measurements made using the overscan pixel values.

3.1 *Data Reduction*

Serial covariance values were calculated from the same set of ≈200 pairs of flat-field images described in Sec. 2.1. This finely sampled set of pairs is well suited for distinguishing features in the covariance curves that occur only over a certain signal range. In the absence of CTI effects and at signal levels below pixel full well, to first order the covariances between adjacent pixels rise quadratically with flat-field signal mean as a result of the brighter-fatter effect. The brighter-fatter effect is named for the observed broadening of source widths with increasing source signal. As charge is accumulated in a pixel, the strength of the repulsive electrostatic force increases, thereby increasing the probability that future excited charges will be deflected into neighboring

Downloaded From: https://www.spiedigitallibrary.org/journals/Journal-of-Astronomical-Telescopes,-Instruments,-and-Systems on 03 Oct 2023
Terms of Use: https://www.spiedigitallibrary.org/terms-of-use

pixels[10] and increasing the covariances between adjacent pixels. This relation is also apparent in photon transfer curve (PTC) measurements where there is a quadratic loss of variance as a function of flux compared to the expected value from Poisson statistics.[9] Due to the signal-dependent deferred charge effects described previously, large deviations from this theoretical behavior are expected to be observed at various values of flat-field signal for several segments.

In order to derive accurate covariance values, care needs to be taken to prevent measurement errors due to other sensor effects. With this in mind, each flat field is preprocessed via an overscan correction, bias frame subtraction, and gain correction. Any detected pixel defects such as bad columns, bright pixels, or dark pixels are masked. As the gains used are derived from the 55Fe measurements, they are not affected by the brighter-fatter terms themselves as are gain measurements from PTC methods, which rely on accurate modeling of the variance term. Pixel covariances are measured on the difference images between flat pairs to remove any additional fixed structure caused by the flat-field illumination pattern.

3.2 *Covariance Calculations*

The pixel covariances of the flat-field images are derived from the resulting processed difference images. In practice, this is determined on the image by storing the nominal array values $s_{m,n}$ of pixel counts (in electrons), calculating $\mathrm{cov}(s_{m,n}, s_{m+i,n+j})$ by shifting the array by i, j, and calculating

$$\mathrm{cov}(s_{m,n}, s_{m+i,n+j}) = \langle (s_{m,n} - \overline{s}_{m,n})(s_{m+i,n+j} - \overline{s}_{m+i,n+j}) \rangle, \tag{5}$$

where $s_{m,n}$ are the counts recorded in pixel (m, n), i.e., the value for the pixel in row m and column n. The image is then shifted and scanned out to the desired lag value. For this study, the figures shown are for the nearest serial neighbor pixel covariance values, or a lag value of $j = 1$ in the serial direction of the CCD.

In the following plots, the calculated covariances are normalized by the mean flat-field signal value of the image. To further reduce the impact of outlier pixels, a 3σ clipping is applied when computing any averages.

The measured normalized serial pixel covariances for each of the segments from ITL CCD R02/S02 are shown in Fig. 7 and demonstrate the relation between the derivative of the deferred charge with respect to signal and covariance described by Eq. (3). The sharp peaks in the covariance plots correspond to the regions with the greatest increase of measured serial CTI shown in Fig. 3, or regions of large positive slope that were attributed to charge trapping.

Both the electronic effects described previously (Sec. 2.1), which produce tails of signal extending many pixels into the serial overscan regions, and the global CTI are largely proportional to the pixel signal; therefore, the contributions of these two effects on the normalized pixel covariances are predicted to be small constant offsets. Both of these contributions to the normalized covariance are degenerate with the true pixel covariances that also scale linearly with signal and therefore cannot be measured directly, unlike the non-linear contributions that can be distinctly identified.

There are also a number of features at low signal level: the majority of the segments in the image show a small upturn in the covariance at low signal, although Seg07 shows a trend toward negative values that may be related to the extreme serial deferred charge signal measured in this segment at similar signal levels. At these signal levels, effects such as read noise correlations and row-by-row gain fluctuations can also become significant contributions to the measured pixel covariances and may account for some of this behavior; however, an in-depth discussion of all features of the covariance curves is beyond the scope of this paper.

Serial covariance measurements can also be used to show that the deferred charge is due to localized charge trapping, independent of the pixel position in the serial direction and on the number of pixel transfers. This is done by calculating the serial pixel covariances as a function of horizontal position. For each sensor segment, the serial covariance calculation is performed once using only pixels located in the first 50 columns and once using only pixels located in the last 50 columns.

Downloaded From: https://www.spiedigitallibrary.org/journals/Journal-of-Astronomical-Telescopes,-Instruments,-and-Systems on 03 Oct 2023
Terms of Use: https://www.spiedigitallibrary.org/terms-of-use

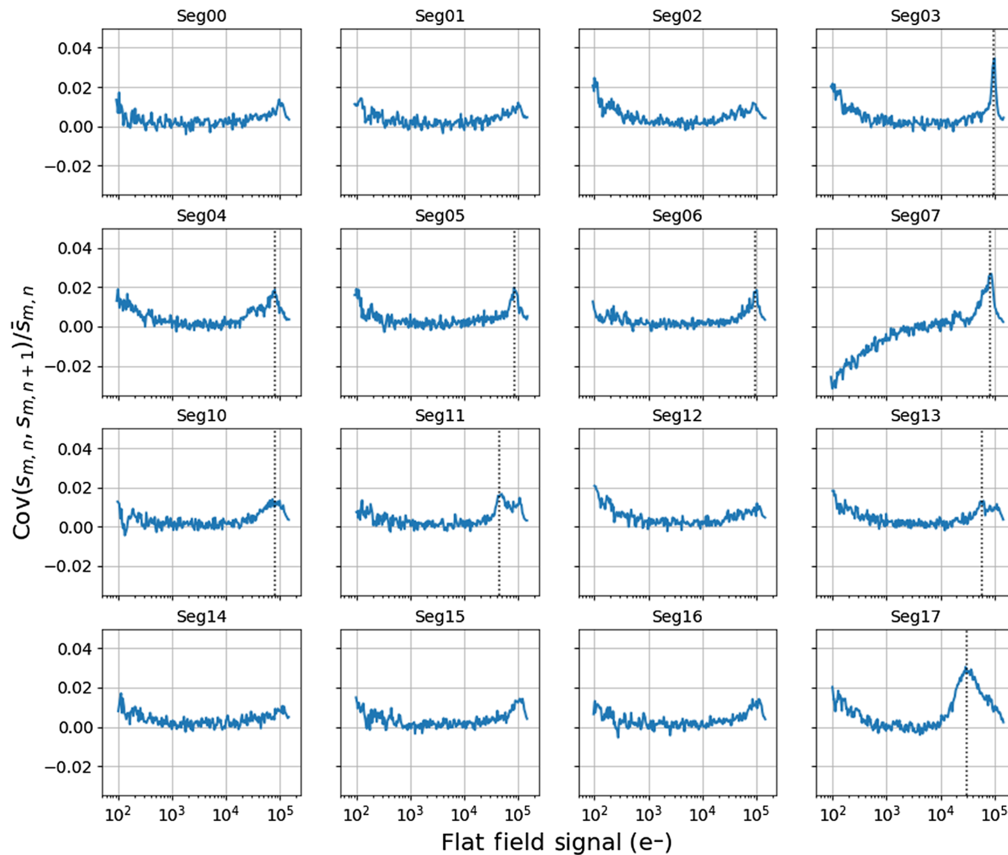

Fig. 7 Normalized serial pixel covariances $\text{cov}(s_{m,n}, s_{m,n+1})/\bar{s}_{m,n}$ for the 16 segments of a single ITL 3800C, calculated using all image pixels. The vertical dotted lines plotted in a set of subplots indicate per-segment signal levels of interest and are reproduced at the same flat-field signal value across Figs. 3, 5, 7, 12, 14, and 18.

Pixels located in the first 50 columns will undergo far fewer serial pixel transfers during the image readout process. The deferred charge caused by global CTI effects that are dependent on the number of pixel transfers should then be much less in these pixels than in pixels located in the last 50 columns. A comparison of the results, shown in Fig. 8, shows that the sharp peaks in the normalized serial pixel covariances associated with increases in serial CTI are approximately equal between the two cases. This is consistent with increased serial pixel covariances caused by deferred charge that occurs at single-pixel location in the serial prescan, rather than global CTI that is dependent on the number of pixel transfers.

3.3 *Science Impact*

The changes to the covariances and variances are of particular concern when measuring and correcting the brighter-fatter effect. In the absence of correction, the dependence of source width on signal level results in biased measurements of the point spread function (PSF) determined from bright stars.[10] In order to perform science at the level of precision required of LSST, PSF modeling errors must be controlled to a high level of precision. Weak lensing measurements require PSF size modeling errors to be controlled at the level of 10^{-3}. The correction method being tested for the Rubin Observatory data reduction pipeline follows the Coulton, Armstrong, Smith, Lupton, and Spergel[11] method that derives a translationally invariant scalar kernel from flat-field image pair covariances. This correction should eliminate the increasing size of spots as a function of signal and restore the linearity of the PTC and model fitting photometry. As the corrected image represents essentially a deconvolution of the pixel values, effects such as irregular jumps from CTI must be corrected to prevent a derived kernel that has features that are not due to brighter-fatter that would lead to an incorrect correction model and a degraded science

Downloaded From: https://www.spiedigitallibrary.org/journals/Journal-of-Astronomical-Telescopes,-Instruments,-and-Systems on 03 Oct 2023
Terms of Use: https://www.spiedigitallibrary.org/terms-of-use

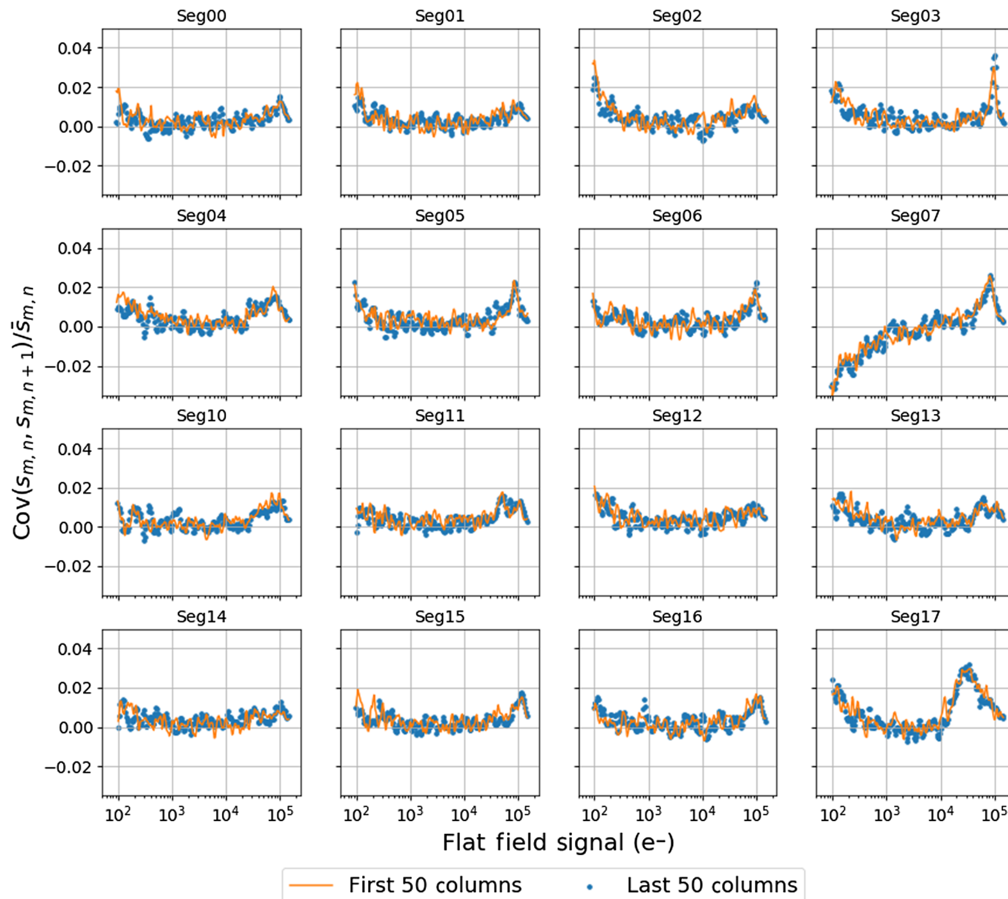

Fig. 8 Normalized serial pixel covariances $\mathrm{cov}(s_{m,n}, s_{m,n+1})/\bar{s}_{m,n}$ for the 16 segments of a single ITL 3800C calculated using only pixels in the first 50 columns and using only pixels in the last 50 columns. In each case, the results have been smoothed with a Gaussian kernel to compensate for the higher noise scatter that results from using less pixel data.

image. Past studies of the correction of LSST images using this method have concluded that substantial improvements of the brighter-fatter effect correction can be made by removing the pixel correlations caused by deferred charge, especially for those ITL segments most severely affected by poor charge transfer.[12]

4 Deferred Charge Forward Algorithm

Development of a deferred charge correction algorithm is divided into two tasks: a forward algorithm to recreate the effects of the deferred charge through simulation of the readout process and a reverse algorithm to remove the deferred charge effects. There are numerous existing algorithms for modeling deferred charge in CCDs; examples include the models developed for deferred charge correction of images from the Hubble Space Telescope (HST) Wide-Field Planetary Camera,[13,14] the HST Advanced Camera for Surveys/Wide Field Channel,[15] and the Gaia space telescope.[16] Many of these existing models were developed to specifically model the global CTI effect of deferred charge due to a large number of radiation-induced traps distributed uniformly throughout the pixel array and/or require extensive knowledge of the sensor implant architecture, doping profiles, voltage operating conditions, and clocking schemes.

The characterization of deferred charge in LSST camera ITL CCDs described in Sec. 2 has shown that the deferred charge caused by global CTI effects is small compared to the deferred charge caused by localized charge trapping by a potential pocket within the serial prescan pixels. Additionally, many details regarding the CCD semiconductor architecture are proprietary,

Downloaded From: https://www.spiedigitallibrary.org/journals/Journal-of-Astronomical-Telescopes,-Instruments,-and-Systems on 03 Oct 2023
Terms of Use: https://www.spiedigitallibrary.org/terms-of-use

making the application of existing detailed device-level simulations very challenging. For these reasons, a new suite of software tools, named CTISIM (https://github.com/Snyder005/ctisim), was specifically developed as an adaptation of the existing phenomenological deferred charge modeling methods to simulate the average deferred charge behavior of LSST camera ITL CCDs.

4.1 *Simulation Workflow*

A limited set of parameters, summarized in Table 2, is used to define a CTISIM model used to create a forward algorithm to simulate the serial readout of a row of pixels. Image pixels $s_{m,n}$ are successively transferred pixel to pixel in the serial direction (corresponding to index n), interacting with any potential pocket traps encountered during the process, and into a final image array where electronic noise and offset effects are added. Each pixel transfer is performed in three steps: charge capture (Sec. 4.2), charge transfer and readout (Sec. 4.3), and charge release (Sec. 4.4). These steps are repeated until the entire pixel array, including the desired number of serial overscan pixels, has been transferred into the final image array. Each row encounters the same serial register, therefore, this process can be performed on each row simultaneously. Because CTISIM only aims to reproduce the average deferred charge behavior, fractional values of charge are allowed for all mathematical operations on pixel signal.

Figure 9 shows a flowchart summarizing the forward algorithm. This algorithm shares inheritance from other deferred charge models, however, the largest difference is that the CTISIM charge capture and release is performed by large localized potential pocket charge traps. Additionally, within the CTISIM framework, the modeling of the deferred charge that occurs at every pixel transfer caused by bulk traps has been reduced to a single parameter b, representing the mean global CTI.

The pixel array to be processed through the CTISIM readout simulation can be initialized from CTISIM software tools based on the GALSIM software package[17] or from existing images that conform to the LSST camera CCD image file formatting. These include simulated LSST camera CCD images created using imSim (https://github.com/LSSTDESC/imSim), a sophisticated simulation package that creates realistic images using information from existing source catalogs and incorporating a number of instrumental effects specific to the LSST camera, and calibration data taken during the LSST camera integration and testing. All operations performed by CTISIM assume pixel signals in units of electrons; therefore, existing images provided to CTISIM must undergo some minor image calibration.

4.2 *Charge Capture*

The charge capture step (Fig. 9, box 3) involves the interaction of the pixel array with the array of potential pocket traps and is the first half of simulating deferred charge due to localized charge

Table 2 Summary of the parameterization of a CTISIM model used by the forward algorithm for simulating deferred charge.

Parameter	Description
O	Global electronic offset
σ_R	Electronic read noise
b	Global CTI
ℓ	Potential pocket trap pixel location
τ_e	Potential pocket trap emission time constant
$q_c(s)$	Potential pocket trap capture function
A_L	Local electronic offset constant of proportionality
τ_L	Local electronic offset decay time constant

Downloaded From: https://www.spiedigitallibrary.org/journals/Journal-of-Astronomical-Telescopes,-Instruments,-and-Systems on 03 Oct 2023
Terms of Use: https://www.spiedigitallibrary.org/terms-of-use

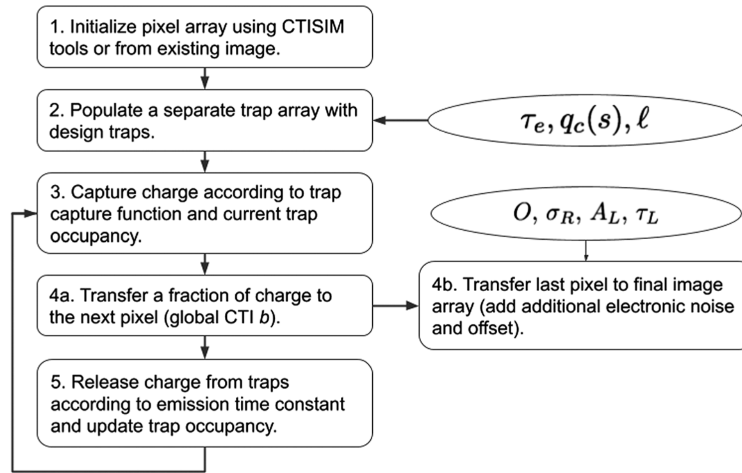

Fig. 9 Flowchart describing the CTISIM forward algorithm for simulating serial deferred charge effects and showing the input model parameters at each step.

trapping. The potential pocket traps in CTISIM are defined by their capture time constant τ_c, emission time constant τ_e, and pixel location ℓ within the serial register, as well as any additional parameters necessary to define the functional form of charge capture selected to represent the trap. For serial transfer, the dwell time t_{dwell} (time spent by the charge cloud in each pixel) is on the order of 1 μs, therefore, it is important to consider the capture time constant τ_c, defined as

$$\tau_c = \frac{1}{\sigma_c n v_{\mathrm{th}}}, \tag{6}$$

where σ_c is the capture cross section, n is the electron concentration, and v_{th} is the thermal velocity. Studies of proton-irradiated CCDs have determined that for typical single electron traps, the trap capture time constants are below 10^{-5} μs.[18] Device level simulations of charge transport have also shown that interphase trapping that occurs on the order of nanoseconds is necessary to fully explain the observed behavior of charge trapping during transfer.[19] Therefore, we adopt the assumption of instantaneous charge capture within CTISIM, though in principal, the probability of charge capture, as a function of the trap capture time constant, could be allowed to vary.

During the charge capture step, a localized charge trap will capture a portion of the charge, determined by the trap's charge capture functions $q_c(s_{m,n})$, from the pixel signal located at the same pixel location as the potential pocket trap. The specification of the trap capture function of each potential pocket trap can be taken from "volume-driven" or "density-driven" models[20] or directly defined from previous measurements via a look-up table. The amount of captured charge is recorded within the trap array as a means to continually monitor the trap occupancy for future steps. Consideration is also made for the current occupancy of the serial trap; previously trapped charge that has not yet been released from the trap will reduce the total amount of charge that the trap can capture.

4.3 *Charge Transfer and Readout*

The charge transfer and readout step (Fig. 9, boxes 4a and 4b) represents the action of serial voltage clocking to transfer charge from one pixel to another and to transfer the last serial pixel to the sense node. It is at this step that the simplified implementation of mean deferred charge due to global CTI loss proportional to pixel signal occurs. During the charge transfer half of this step, the pixel signal (not considering the portion that has been previously captured by potential pocket traps) is divided into "transferred charge" and "stationary charge," $s_{m,n} = as_{m,n} + bs_{m,n}$, where b is the global CTI value and $a = 1 - b$. The "transferred charge" as_n is then shifted over

Downloaded From: https://www.spiedigitallibrary.org/journals/Journal-of-Astronomical-Telescopes,-Instruments,-and-Systems on 03 Oct 2023
Terms of Use: https://www.spiedigitallibrary.org/terms-of-use

one pixel column and combined with the "stationary charge" $bs_{m,n-1}$ component of the preceding pixel, in order to obtain the updated pixel values after a single serial transfer (Fig. 9, box 4a).

The charge readout step represents the transfer of the last serial pixel charge to the sense node and the action of the readout electronics to measure the pixel signal (Fig. 9, box 4b). During this step, the "transferred charge" fraction of the last serial pixel along with signal contributions from Gaussian distributed read noise σ_R and electronic offsets are combined and used to populate the final image array.

The electronic offset contribution has two components: a global offset value O that is constant across the entire pixel array and a local offset value that varies from pixel-to-pixel. The CTISIM model for the local electronic offset is a coupling between the pixel charge at the sense node and the silicon bulk substrate implemented as an increase to the electronic offset value that is proportional to the pixel signal and that decays exponentially with some characteristic timescale. Consider the exponentially decreasing sequence described in Eq. (7), where A_L represents the scaling of the effect with pixel signal, τ_L represents the characteristic time of decay, and t represents the pixel transfer time:

$$(A_L s_{m,n-j} e^{-jt/\tau_L} : j = 0, 1, 2, \dots). \tag{7}$$

Each term in the sequence represents a possible signal contribution to the current pixel s_n, due to the influence of all preceding pixels s_{n-j}, including the current pixel itself; the total signal contribution to the current pixel can either be the summation of this sequence or the maximum element of the sequence. Both options will recreate the exponentially decreasing long tails of signal in the serial overscan region described in Sec. 2.1, though the former will result in a rise in signal across the first several columns of a flat-field image that has not been observed currently. Therefore, in the CTISIM model, for each pixel, only the largest element of the sequence in Eq. (7) is taken to be the local electronic offset contribution, i.e., for a given local electronic offset determined by a pixel signal, the subsequent pixel signal can either: increase the offset if it is higher, maintain the offset if it is equal, or decrease the offset if it is lower either through the decay of the original offset or by explicitly setting a newer, lower offset.

4.4 *Charge Release*

The final step of the simulated pixel transfer is the charge release step (Fig. 9, box 5), where charge that was previously captured through interactions with the potential pocket trap array is now released back into the pixel array. The amount of charge released by the potential pocket traps q_r is determined by the trap's current occupancy q and emission time constant τ_e:

$$q_r = q(1 - e^{-t/\tau_e}). \tag{8}$$

The potential pocket trap occupancy values are again updated to reflect the charge released, and the entire simulated serial pixel transfer process is ready to be repeated.

5 Deferred Charge Reverse Algorithm

The reverse algorithm refers to the process in which charge is returned to its original position, removing both deferred charge signal tails in the overscan pixels and the corresponding impact on pixel covariance measurements. A true inversion of the image mapping caused by the deferred charge effects is not analytically possible without knowing the original pixel values; instead a common method is to use the iterative application of the forward algorithm to generate a reverse algorithm, detailed by Massey et al.[13] This is equivalent to running the full CTISIM forward algorithm for at least one iteration on each image to be used to produce a corrected image. The number of iterations should be minimized because each successive iteration will introduce additional correlations due to the contribution of "untrailed" read noise,[20] which can further degrade the accuracy of the brighter-fatter kernel.

Downloaded From: https://www.spiedigitallibrary.org/journals/Journal-of-Astronomical-Telescopes,-Instruments,-and-Systems on 03 Oct 2023
Terms of Use: https://www.spiedigitallibrary.org/terms-of-use

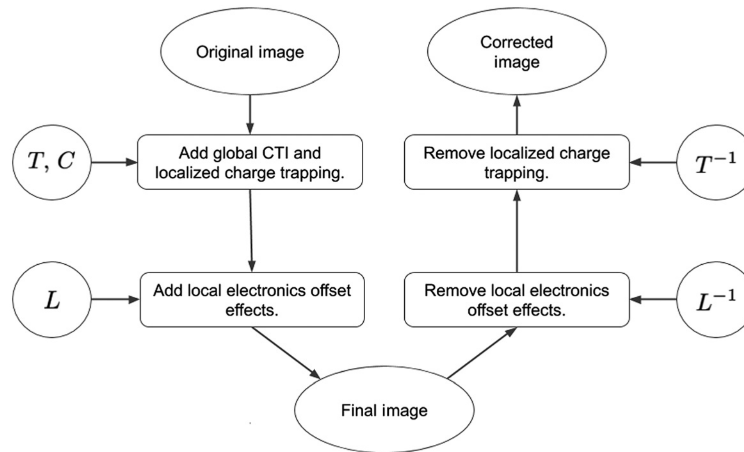

Fig. 10 Flowchart describing the reverse algorithm for removing deferred charge effects using a series of mathematical operators. On the left side, the downward flow describes an estimate of the CTISIM forward model in terms of a set of mathematical operators. On the right side, the upward flow describes the use of the inverse of these operators as the basis for a reverse algorithm. Images are corrected for the local electronic offset effect and localized charge trapping, but not for the effect of global CTI; as such the corrected image is not equal to the original image.

Due to the relative simplicity of the observed deferred charge in LSST CCDs compared to radiation-damaged CCDs (one large localized charge trap versus a distribution of multiple families of bulk traps), it is possible to replace the computationally expensive task of a full CTISIM forward algorithm with a series of mathematical operators that estimate each software step of the forward algorithm, to transform the pixel values in an image row $s_{m,n} \mapsto s'_{m,n}$, allowing for a 100-fold increase in computational speed. Deferred charge correction can then be performed by replacing the full CTISIM forward algorithm with the mathematical operators in the forward iterative method or through direct application of the inverse mathematical operators. Here we outline the later method as the reverse algorithm for correcting deferred charge in LSST CCD images.

A flowchart of the reverse algorithm derived from the CTISIM forward algorithm operators to remove the effects of deferred charge is shown in Fig. 10.

It is important to note that we are only concerned with removing the deferred charge caused by localized charge trapping due to a serial register potential pocket trap and the local signal-dependent electronic offset effect and not the deferred charge effects due to global C TI. This is due to the fact that parameterization of the CTISIM forward algorithm can only reproduce the average effect of the global CTI, though this average effect could be removed in cases where the remaining deferred charge from global CTI is above the 5×10^{-6} desired level.

5.1 *Local Electronic Offset Correction*

The signal contributions of a local signal-dependent electronic offset occur after charge redistribution due to trapping and transfer inefficiency and thus must be removed first. Using Eq. (7) that describes the CTISIM electronic offset implementation, the local electronic offset operator L on pixel signals $s_{m,n}$ is exactly given by

$$L[s_n] = s_n + \max(A_L s_{m,n}, A_L s_{m,n-1} e^{-t/\tau_L}, \dots A_L s_{m,n-j} e^{-jt/\tau_L}). \tag{9}$$

The sequence of terms within the max operator can be extended to encompass all previous pixel signals; however, it is more suitable to truncate the sequence at an appropriate value of j at which the terms fall below a specified threshold (e.g., 0.1 electrons).

Downloaded From: https://www.spiedigitallibrary.org/journals/Journal-of-Astronomical-Telescopes,-Instruments,-and-Systems on 03 Oct 2023
Terms of Use: https://www.spiedigitallibrary.org/terms-of-use

From Eq. (9), an inverse electronic offset operator L^{-1} can be calculated as

$$\begin{aligned} L^{-1}[s'_{m,n}] &= s'_{m,n} - \max(A_L s_{m,n}, A_L s_{m,n-1} e^{-t/\tau_L}, \cdots A_L s_{m,n-j} e^{-jt/\tau_L}) \\ L^{-1}[s'_{m,n}] &\approx s'_{m,n} - \max(A_L s'_{m,n}, A_L s'_{m,n-1} e^{-t/\tau_L}, \cdots A_L s'_{m,n-j} e^{-jt/\tau_L}) + \mathcal{O}(A_L^2 s'_{m,n}). \end{aligned} \tag{10}$$

In the second line of Eq. (10), the substitution of the known primed pixel values as an estimator for the unknown original (unprimed) pixel values introduces an error term dependent on the square of the constant of proportionality of the local electronic effect A_L.

5.2 *Potential Pocket Trap Deferred Charge Correction*

Determination of a suitable operator T that describes charge capture and release caused by potential pocket traps and its inverse T^{-1} is far more complicated. The first simplifying assumption made is that all charge captured in a pixel is released into the pixel immediately following it. The strength of this assumption is dependent on the potential pocket trap emission time constant. Previous estimates of the emission time constant of low signal charge trapping in LSST CCDs have resulted in values of τ_e between 0.8 and 1.0 μs, or equivalently, >90% of trapped charge being released after one pixel transfer.[8] The large non-linear behavior of the mean signal in the first serial overscan pixel resulting from the localized charge trapping is also largely absent in the second and third serial overscan pixels (Fig. 5), providing support for emission time constant values that allow for the majority of captured charge to be released into the following pixel. Thus this is an acceptable approximation for the majority of the observed deferred charge from localized charge trapping, though improvements to this may be necessary to deal with those CCD segments where this may not be sufficient (Seg07 and Seg17 in Fig. 5).

Because the pixel transfer step that introduces the global CTI effects occurs between the charge capture and charge release steps, the localized charge trapping operator is coupled to the global CTI operator C. For simplicity, we first consider the case where the global CTI is zero, i.e., $b = 0$ in the CTISIM parameterization and $C[s_{m,n}] = s_{m,n}$. The localized charge trapping operator can then be calculated, using Eq. (2), as

$$T[s_{m,n}] = s_{m,n} + q_c(s^*_{m,n-1}) - q_c(s^*_{m,n}), \tag{11}$$

where $q_c(s_{m,n})$ is the potential pocket trap charge capture function [analogous to ϵ in Eq. (2)]. Although $s_{m,n}$ is the initial pixel signal, and $s'_{m,n}$ is the transformed pixel signal, $s^*_{m,n}$ describes an intermediate pixel signal state, before charge capture but after charge redistribution that has occurred during all preceding pixel transfers. It is the determination of $s^*_{m,n}$ that requires knowledge of the original pixel signal values because of its dependence on all previous pixel values and trap occupancies.

Now we consider the case of a non-zero value for global CTI, or $b \neq 0$ in the CTISIM parameterization, shown in the following equation:

$$T[s_{m,n}] = C[s_{m,n}] + a q_c(s^*_{m,n-1}) - a q_c(s^*_{m,n}) + \mathcal{O}(b q_c(s^*_{m,n})). \tag{12}$$

The first term refers to the initial pixel signals transformed by the global CTI operator C, the second term and third terms are the charge redistribution described in Eq. (11) now modulated by $a = 1 - b$, and the final term represents cross terms between the global CTI and the localized charge trapping, the largest of which is of order $b q_c(s_{m,n})$.

Instead of a full inversion to solve for $s_{m,n}$, Eq. (12) is used to solve for $C[s_{m,n}]$. This is equivalent to removing the localized charge trapping from a potential pocket trap while leaving global CTI:

$$\begin{aligned} T^{-1}[s'_{m,n}] = C[s_{m,n}] \quad T^{-1}[s'_{m,n}] &\approx s'_{m,n} - a q_c(s^*_{m,n-1}) + a q_c(s^*_{m,n}) \\ T^{-1}[s'_{m,n}] &\approx s'_{m,n} - a q_c(s'_{m,n-1}) + a q_c(s'_{m,n}) + \mathcal{O}(q_c(q_c(s_{m,n}))). \end{aligned} \tag{13}$$

Using the known final pixel values $s'_{m,n}$ as an estimate in the third line of Eq. (13) for the unknown $s^*_{m,n}$ pixel values, an error term of order $q_c(q_c(s_{m,n}))$ is introduced. For the majority

Downloaded From: https://www.spiedigitallibrary.org/journals/Journal-of-Astronomical-Telescopes,-Instruments,-and-Systems on 03 Oct 2023
Terms of Use: https://www.spiedigitallibrary.org/terms-of-use

of the measured deferred charge behavior this is an acceptable estimate, though there is some evidence that a more robust estimate obtained from a calculation of $s^*_{m,n}$ to higher order may be needed.

5.3 *Global CTI Correction*

A correction of the mean global CTI effects can be performed using the global CTI operator C, the simplest estimate of which is a binomial approximation of the operator as

$$C[s_{m,n}] \approx (1 - N_T(n)b)s_{m,n}, \tag{14}$$

where $N_T(n)$ is the number of transfers for each pixel, dependent on the pixel index n. Higher-order estimates of C include contributions from preceding pixels, modulated by powers of b and a, and can be calculated to arbitrary order, if desired. The use of the global CTI operator C or inverse operator C^{-1} has not been applied to the results presented in Sec. 7 because of the limitation of only being able to measure the mean global CTI effects accumulated over the full course of the serial read-out rather than charge capture and release occurring at a well-defined location within the serial register, as is the case for localized charge trapping. This correction could be used to further reduce deferred charge effects in segments where the global CTI is above the desired 5×10^{-6}.

6 Parameter Determination from Data

Determination of a suitable CTISIM model parameterization (Table 2) that can reproduce the overscan pixel data is required for the calculation of the inverse operators L^{-1} and T^{-1}, described in Sec. 5, used for the deferred charge correction through direct application to the pixel data. The determination of a best-fit CTISIM model is made by minimization of the sum of the χ^2 over serial overscan pixels $n > n0$, where n_0 is the number of imaging columns plus serial prescan columns, following flat fields with signal levels S:

$$\chi^2 = \sum_S \sum_n \frac{[D(n,S) - M(n,S)]^2}{\sigma(n,S)^2}, \tag{15}$$

where $D(n,S)$ is the experimental flat-field image serial overscan pixel data and $M(n,S)$ is simulated flat-field image overscan pixel data generated from a CTISIM model. For the both $D(n,S)$ and $M(n,S)$, we determine the mean serial overscan pixel value for each pixel n by taking the mean over all rows m. A single joint-fit of the overscan pixel data to a CTISIM model to determine the full parameterization is only possible in the simplest of cases. There is substantial degeneracy between the pixel signal contribution of the local electronic offset effect and the deferred charge caused by global CTI; both are linear with pixel signal, but the contribution of global CTI to the overscan pixel signals decays more quickly. Additionally, the capture function $q_c(s)$ of the potential pocket traps must also be known *a priori*, or approximated well by a predetermined functional form, which is often not the case.

Instead, we apply a divide-and-conquer strategy where the parameterization of each of the CTISIM model components (global CTI, electronic effects, and localized charge trapping) is found through best-fit determinations performed on three separate datasets (separated by different ranges of flat-field signals S and overscan pixels n) where the effects of the different sources of deferred charge signal are the largest. Figure 11 shows a summary flowchart of this process and the parameters determined at each step. First, the contribution from local electronics offset effects is determined (Fig. 11, box 1). Next, we determine the linear component of the overscan pixel signals as a function of flat-field signal, assumed to be the global CTI contribution, using a second chi-square minimization (Fig. 11, box 2). Finally, the residual overscan pixel signal, after removing the contributions of the electronic effects and global CTI using the partial parameterization obtained in the previous steps, is used to create a look-up table of the capture function $q_c(s)$ for the localized charge trapping.

Downloaded From: https://www.spiedigitallibrary.org/journals/Journal-of-Astronomical-Telescopes,-Instruments,-and-Systems on 03 Oct 2023
Terms of Use: https://www.spiedigitallibrary.org/terms-of-use

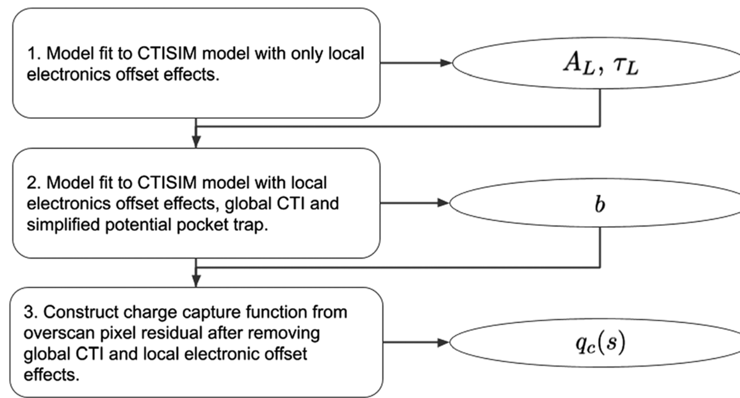

Fig. 11 Flowchart describing the procedure to determine the CTISIM model parameters to be used by the deferred charge correction algorithm.

In this section, overscan data from flat-field images taken with ITL CCD R02/S02 are used to demonstrate the process of determination of a best-fit CTISIM model in more detail and the application of the reverse algorithm to correct the effects of deferred charge. The data set used for $D(n, S)$ in the χ^2 minimization process is the same set of calibrated flat-field images described in Sec. 2.1 that was used for the deferred charge characterization. Because this data set consisted of pairs of flat-field images taken at each signal level, one set of flat-field images was used in the determination of the CTISIM model parameterization, whereas the other set of flat-field images was used in calculations of serial CTI used to verify and test the correction algorithm (Sec. 7). Calculations of the serial pixel covariances after correction required the use of both flat-field images in each pair.

6.1 *Determination of Local Electronic Offset Parameterization*

The degeneracy between the signal-dependent local electronic offset effect and the global CTI can be broken by restricting the overscan pixels used for the χ^2 minimization. The long timescale for the decay of the local electronic offset results in measurable pixel signal contributions extending many pixels into the overscan region (see Fig. 4), and the effect of the global CTI is largest in the first overscan pixel and drops rapidly to zero in the following overscan pixels.

Determination of the parameters A_L and τ_L that set the behavior of the signal-dependent electronic offset effect is performed first through the minimization of Eq. (15) over all flat-field signals S and overscan pixels $n > n_0 + 2$. The model used to generate $M(s, N)$ for this minimization is a CTISIM model that includes only a local electronics offset effect, no global CTI ($b = 0.0$), and no potential pocket traps. The parameter results for this best-fit process for ITL CCD R02/S02 are summarized in Table 3.

There is a large amount of consistency between the best-fit parameters results across all CCD segments with only one outlier Seg07. The values for the local electronic offset effect constant of proportionality A_L that sets the linear dependence range from 1.3×10^{-4} and 2.0×10^{-4}, whereas the values for the characteristic decay time constant of the local electronic offset effect range from 4.5 to 5.5 μs (roughly 2.25 and 2.75 serial pixel transfers).

6.2 *Determination of Global CTI Parameterization*

For the majority of CCD segments, in flat-field images with signals $S < 10,000$ electrons, the overscan pixel signal not resulting from electronic effects appears to only be caused by global CTI. The determination of the global CTI parameter b for all segments is done by a χ^2 minimization over flat-field signals $S < 10,000$ electrons and the first two overscan pixels $n = n_0 + 1$, $n_0 + 2$. The CTISIM model used for this second minimization includes the local electronic offset effect with parameterization fixed to the values determined previously, global

Downloaded From: https://www.spiedigitallibrary.org/journals/Journal-of-Astronomical-Telescopes,-Instruments,-and-Systems on 03 Oct 2023
Terms of Use: https://www.spiedigitallibrary.org/terms-of-use

Table 3 CTISIM model parameter results for ITL CCD R02/S02.

Segment	A_L	τ_L (μs)	b
Seg00	1.5×10^{-4}	5.4	4.6×10^{-7}
Seg01	1.7×10^{-4}	5.1	6.4×10^{-7}
Seg02	2.0×10^{-4}	4.8	7.1×10^{-7}
Seg03	1.6×10^{-4}	5.1	7.3×10^{-7}
Seg04	1.6×10^{-4}	5.0	6.4×10^{-7}
Seg05	1.6×10^{-4}	5.1	7.6×10^{-7}
Seg06	1.8×10^{-4}	5.1	6.1×10^{-7}
Seg07	4.5×10^{-4}	3.4	5.1×10^{-7}
Seg10	1.8×10^{-4}	5.2	4.8×10^{-7}
Seg11	1.6×10^{-4}	5.3	6.3×10^{-7}
Seg12	1.7×10^{-4}	5.1	1.1×10^{-6}
Seg13	1.7×10^{-4}	5.1	7.7×10^{-7}
Seg14	1.8×10^{-4}	5.0	7.1×10^{-7}
Seg15	1.7×10^{-4}	5.1	5.8×10^{-7}
Seg16	1.5×10^{-4}	5.5	3.8×10^{-7}
Seg17	1.3×10^{-4}	4.5	4.9×10^{-6}

CTI b that is allowed to vary, and a linear charge trapping model [Eq. (16)] parameterized by a constant of proportionality A_{trap} and saturation value $q_{\max}$, which are allowed to vary

$$q_{c,\text{linear}}(s_n) = \max(q_{\max}, A_{\text{trap}} s_n). \tag{16}$$

The inclusion of a serial charge trap is necessary to account for segments such as Seg07 and Seg17 in Fig. 3 that have an additional amount of constant deferred charge that can be approximated by this simple linear charge trapping model. The results for global CTI b from this second χ^2 minimization are shown in Table 3, with most segments having global CTI $< 10^{-6}$. The parameter results for the linear trap capture model are not shown for reasons that will be discussed in the following section.

6.3 *Determination of Localized Charge Trapping*

In principal, following the determination of the global CTI parameter b, a full CTISIM model that is valid for signal levels below 10,000 electrons has been determined. However, it is impossible to extrapolate the linear charge trapping model $q_{c,\text{linear}}$ used previously to encompass the non-linear behavior that occurs at higher signal levels. Instead, determination of the potential pocket trap charge capture function $q_c(s)$ that determines the amount of localized charge trapping across all signal levels is done by measuring the remaining signal in overscan pixels after removing the contributions from the local electronic offset effect and the global CTI, and recording the result as a look-up table for $q_c(s)$. This will replicate the previously determined linear trap capture model behavior at low signal and directly measure the non-linear behavior at higher signal.

For each CCD segment, we construct a CTISIM model with the corresponding best-fit parameterization determined by the preceding two best-fits (Table 2) and calculate a difference image between each flat-field image in the experimental data set and a flat-field image generated using the CTISIM forward algorithm. The summed residual signal in the first two overscan

Downloaded From: https://www.spiedigitallibrary.org/journals/Journal-of-Astronomical-Telescopes,-Instruments,-and-Systems on 03 Oct 2023
Terms of Use: https://www.spiedigitallibrary.org/terms-of-use

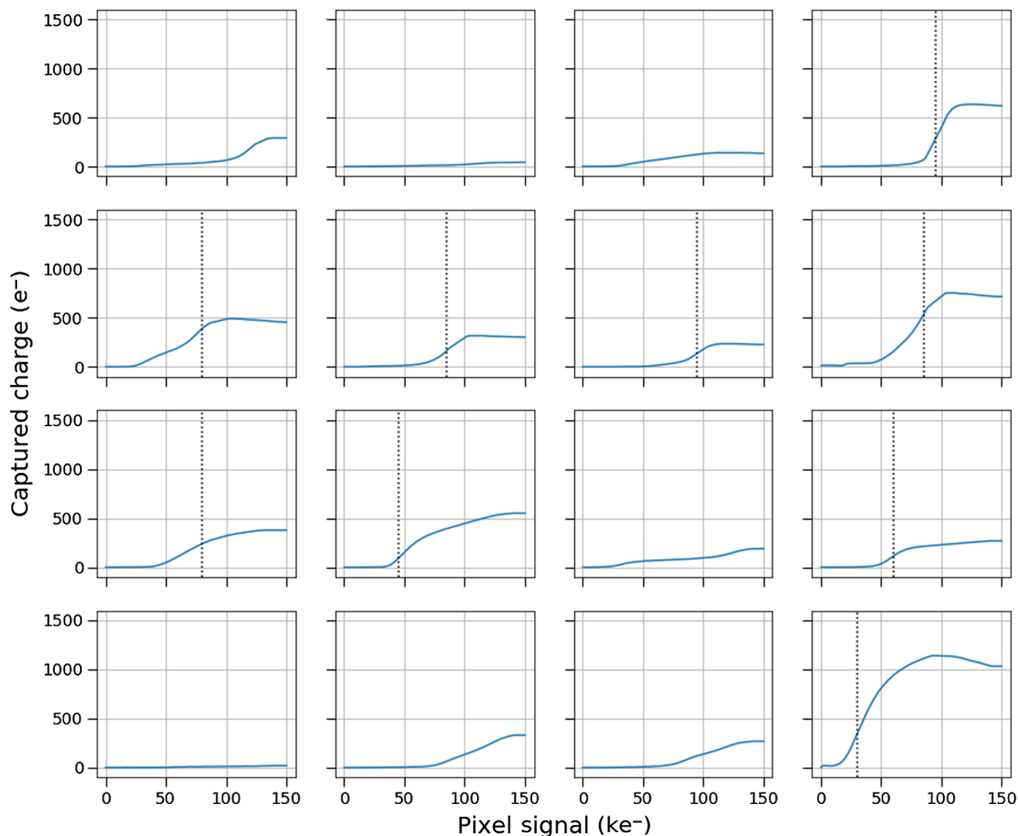

Fig. 12 Potential pocket trap charge capture functions $q_c(s)$ for the 16 segments of ITL CCD R02/S02. The vertical dotted lines plotted in a set of subplots indicate per-segment signal levels of interest and are reproduced at the same flat-field signal value across Figs. 3, 5, 7, 12, 14, and 18.

pixels of the difference image of the two flat-field images, each with signal S, is a direct measurement of the charge capture function $q_c(s)$.

Figure 12 shows potential pocket trap charge capture functions estimated for all of the segments of ITL CCD R02/S02 that serve as the $q_c(s)$ look-up tables with the same signal spacing as the illumination of the flat-field images used in the deferred charge model determination: uniform in log space from 100 electrons to above 150,000 electrons. These capture functions most closely resemble sigmoid functions, showing an increasing amount of captured charge that "rolls off" at higher signal. This is most likely caused by the precise behavior of the electron density of the charge cloud as it encounters the potential pocket. Another important feature of the results for this calculation of $q_c(s)$ is that in some cases, such as for Seg17, the charge capture function is not strictly increasing. This behavior is caused by remaining degeneracy between the linear behavior of the global CTI and linear behavior of the charge capture function at low signal levels that results in an overestimation of the global CTI parameter b and an underestimation of the charge capture function. Unfortunately, this degeneracy also exists in the pixel covariances as a function of pixel signal, as both the global CTI and linear charge trapping will result in a constant for the derivative term in Eq. (3). Future work will focus on determining a method to break this degeneracy in order to improve the correction of the deferred charge caused by localized charge trapping by serial potential pocket traps.

6.4 *Parameter Results Summary*

Figure 13 shows distribution of the parameter results for all of the segments of ITL CCDs installed during the partial focal plane testing period. The results show the largely consistent behavior of the localized electronic offset effect, parameterized by A_L and τ_L, across all of the ITL CCD segments. For a small number of segments, the parameter fits failed to converge. These segments represent extreme cases of deferred charge behavior primarily in segments whose output

Downloaded From: https://www.spiedigitallibrary.org/journals/Journal-of-Astronomical-Telescopes,-Instruments,-and-Systems on 03 Oct 2023
Terms of Use: https://www.spiedigitallibrary.org/terms-of-use

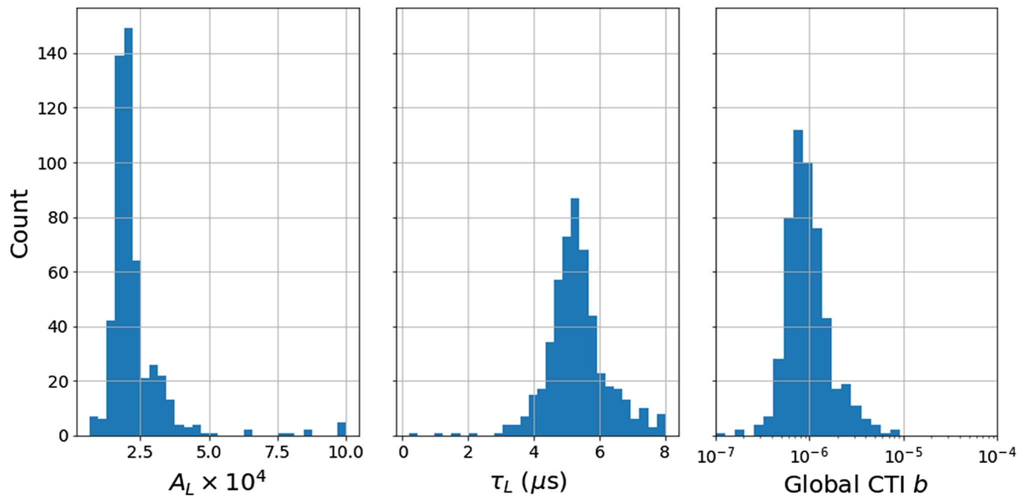

Fig. 13 Distributions of the best-fit CTISIM parameter results (A_L, τ_L, and b) for all ITL CCD segments (576) tested during the partial focal plane testing period.

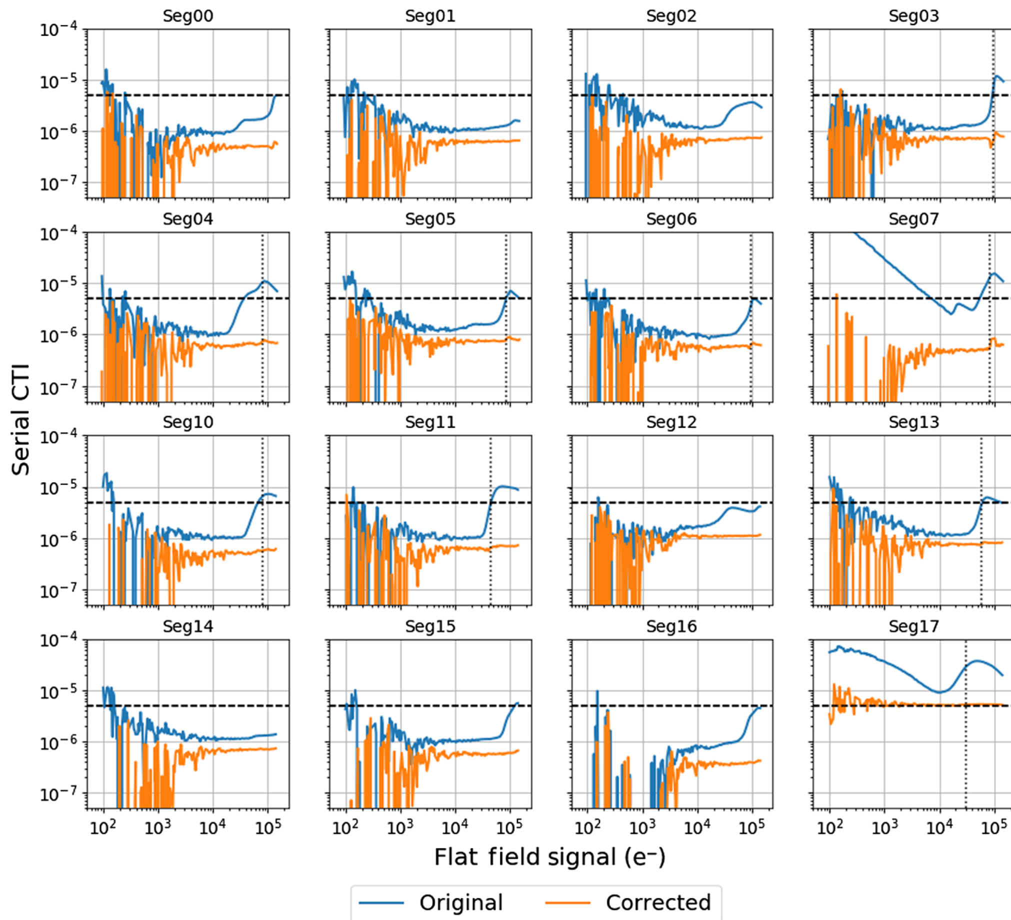

Fig. 14 Serial CTI calculated using the EPER method for the 16 segments of a single ITL STA3800C CCD before (blue) and after correction using the deferred charge reverse algorithm (orange). In both cases, the sum of the signal in the first two serial overscan pixels was used as the numerator in the CTI ratio equation. Below flat-field signals of 10^3 electrons the serial overscan pixel signal becomes subdominant to the read noise. The vertical dotted lines plotted in a set of subplots indicate per-segment signal levels of interest and are reproduced at the same flat-field signal value across Figs. 3, 5, 7, 12, 14, and 18.

Downloaded From: https://www.spiedigitallibrary.org/journals/Journal-of-Astronomical-Telescopes,-Instruments,-and-Systems on 03 Oct 2023
Terms of Use: https://www.spiedigitallibrary.org/terms-of-use

amplifiers are located on the edge of CCD. Seg07 and Seg17 from ITL CCD R02/S02, whose single CCD results are shown throughout this paper, are two examples of similar behavior.

7 Testing the Correction Algorithm

Verification and testing of the deferred charge correction was done by calculating the serial CTI and the serial pixel correlation of flat-field images for ITL CCD R02/S02 that have been corrected using the reverse algorithm outlined in Sec. 5.

7.1 *EPER Measurements After Correction*

Figure 14 shows the serial CTI results for the flat-field images that were corrected using the reverse algorithm. These images were the set of flat-field images that were not used to determine the CTISIM model parameterization. The signal in the first two serial overscan pixels

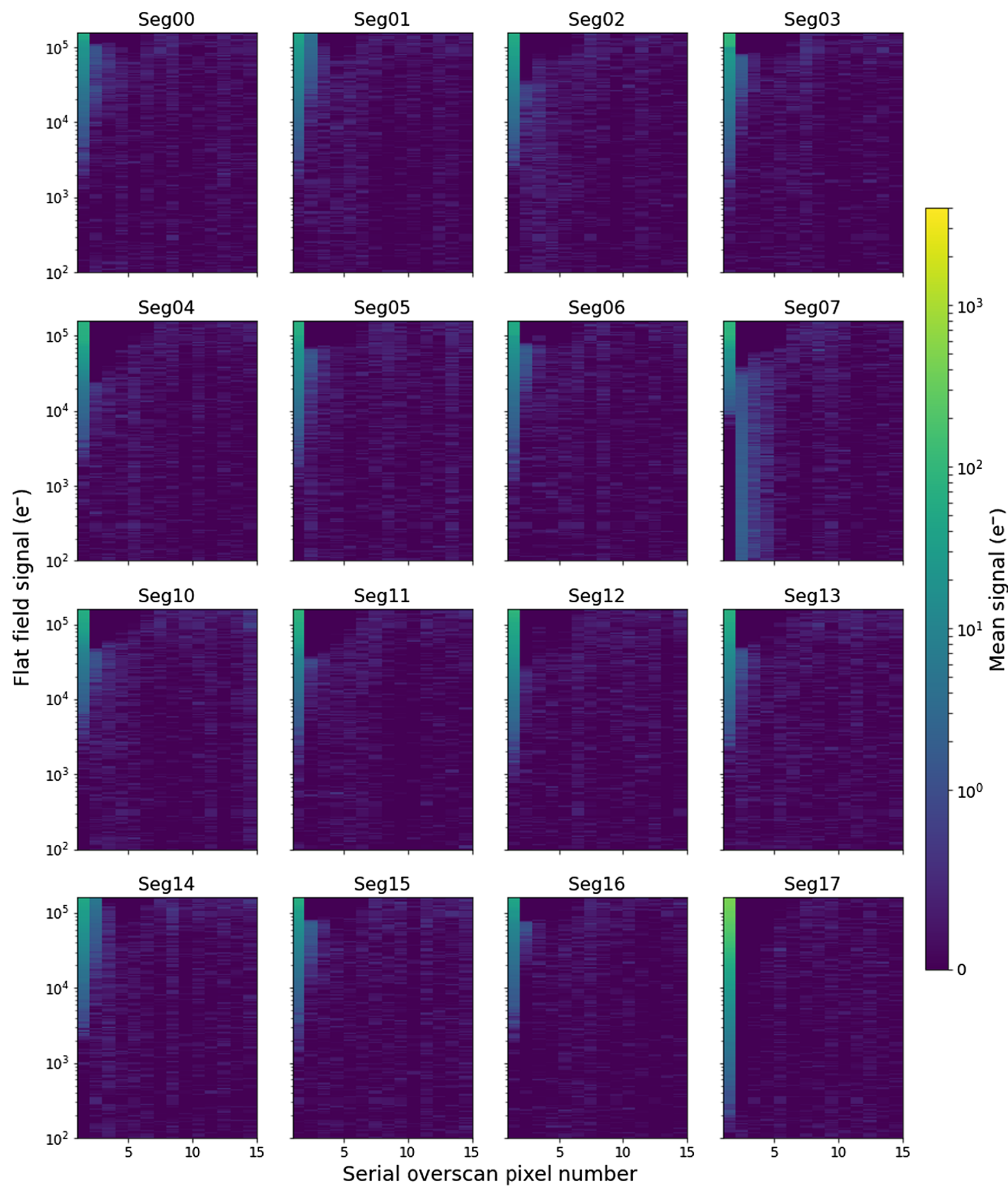

Fig. 15 Mean signal in serial overscan pixels after a corrected flat-field image (displayed on a symmetric log color scale with linear cutoff of 1.0 electron), for flat-field signal levels from 100 to 150,000 electrons, for each CCD segment. Error on the mean signal is 0.14 electrons.

Downloaded From: https://www.spiedigitallibrary.org/journals/Journal-of-Astronomical-Telescopes,-Instruments,-and-Systems on 03 Oct 2023
Terms of Use: https://www.spiedigitallibrary.org/terms-of-use

was used as the numerator in Eq. (1) and the mean of the results for each row in the pixel array was taken, as was the case for the corresponding serial CTI plot for the original, uncorrected data (Fig. 3).

After application of the deferred charge correction to the flat-field images, the large increases in serial CTI associated with the additional deferred charge caused by localized charge trapping have been removed. The remaining signal in the first two overscan pixels of each segment is the linear component caused by global CTI, resulting in a roughly constant value of CTI approximately equal to the parameter b used in each segment's CTISIM model. A few segments show small residual wiggles in the measured serial CTI (e.g., Seg03 at 90,000 electrons) possibly caused by the use of the known final pixel values $s'_{m,n}$ as an estimator during the correction of the localized charge trapping. These residuals appear only in cases where the amount of captured charge $q_c(s)$ is very large and changes rapidly with increasing signal.

Figure 15 shows a reproduction of Fig. 4 using the overscan pixel data from the corrected flat-field images in order to demonstrate the ability for the deferred charge reverse algorithm to remove the signal contributions of the local electronic offset effect. The long tails of signal that were previously observed extending far into the serial overscan pixels have been removed in the corrected flat-field images and only deferred charge signal remains in the first two overscan pixels for all segments except for Seg07. This segment remains an outlier even after correction; in particular, the correction process appears to have caused an under correction of the second and third overscan pixels at low signal levels and an over correction at high signal levels. Further study of this segment and other segments with similar behavior is necessary in order to improve the ability to correct for the most extreme cases of deferred charge.

Figure 16 shows the distribution of serial CTI values calculated using the EPER method for all segments of the ITL CCD sensors, after deferred charge correction, at four different

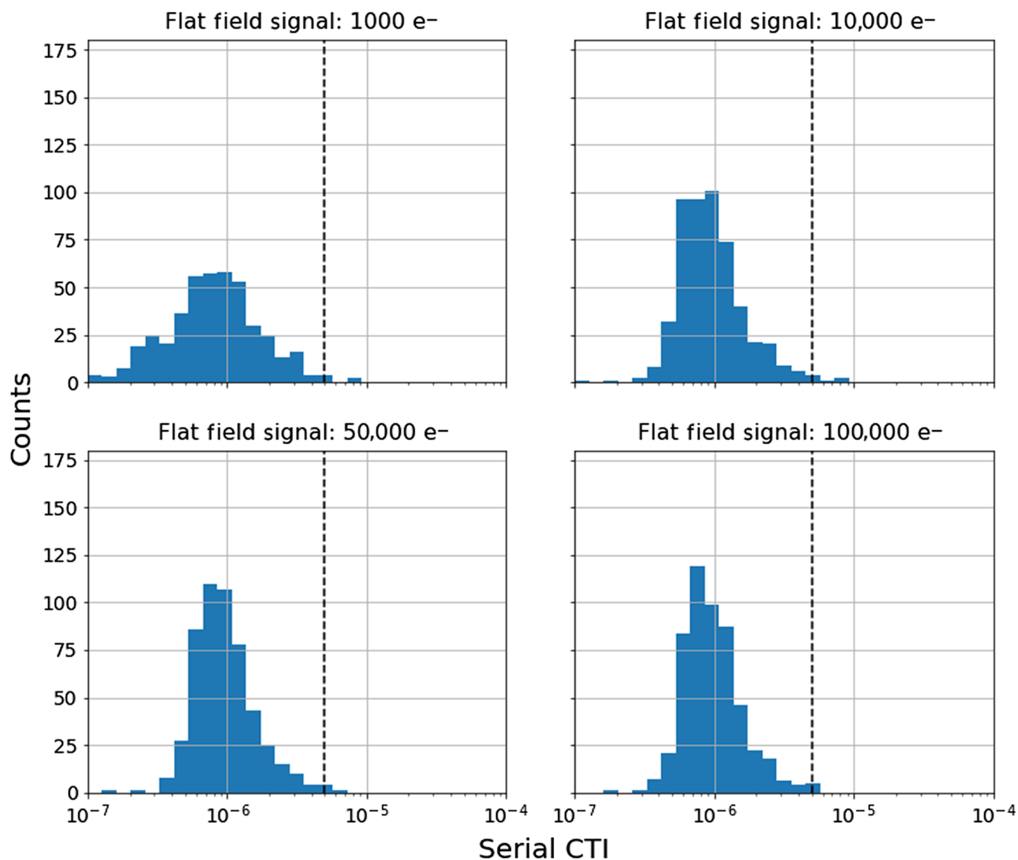

Fig. 16 Histogram of serial CTI values for all ITL CCD segments during the partial focal plane testing period measured using the EPER method from flat-field images taken at four different signal levels after deferred charge correction. The vertical dashed line represents the desired maximum serial CTI value of 5×10^{-6}.

Downloaded From: https://www.spiedigitallibrary.org/journals/Journal-of-Astronomical-Telescopes,-Instruments,-and-Systems on 03 Oct 2023
Terms of Use: https://www.spiedigitallibrary.org/terms-of-use

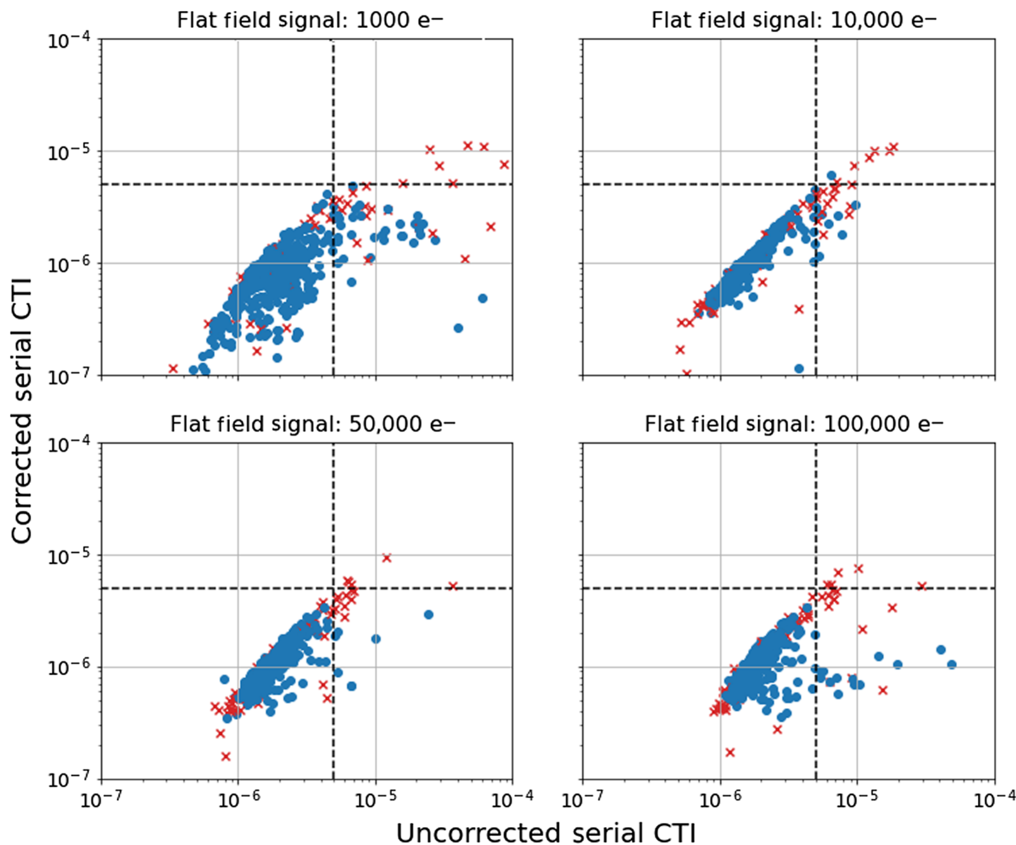

Fig. 17 Scatter plot of the measured serial CTI for each ITL CCD segment during the partial focal plane testing before and after deferred charge correction. The vertical and horizontal dashed lines represent the desired maximum serial CTI value of 5×10^{-6}. Measurements made for Seg07 and Seg17 are plotted as red crosses while all other segment results are plotted as blue circles.

flat-field signal levels. A scatter plot comparison of the new serial CTI results to the original serial CTI results derived from the uncorrected images is shown in Fig. 17. After deferred charge correction, the presence of CCD segments with serial CTI above the desired value of 5×10^{-6} has been almost entirely eliminated and the distributions have been shifted to lower values of serial CTI.

The results of the application of the deferred charge correction to the ITL CCD segments installed in the LSST camera during the partial focal plane testing period have demonstrated the ability to remove the majority of elevated serial deferred charge effects, with only a small number of remaining outlier that are largely results from Seg07 and Seg17 (indicated as red crosses in Fig. 17), which are segments that are located on the edge of the CCD. The proximity of the output amplifier to guard drain (scupper) voltage likely results in changes to behavior of the local electronic offset or any charge trapping by an electrostatic potential pocket trap in the serial register. The result is these effects being more strongly degenerate (linear in signal) and more difficult to separate from each other.

7.2 *Serial Covariance Measurements After Correction*

Measurements of the serial pixel covariances calculated from the corrected flat pairs provide a semi-independent method to verify the performance of the deferred charge correction. Although the CTISIM model parameterization for each segment was calculated using the flat-field overscan pixel information, the serial pixel covariances are calculated using the imaging pixels. The results, shown in Fig. 18, were calculated using the same procedure outlined in Sec. 3 and can be compared to the corresponding results for the original flat pair images (Fig. 7).

Downloaded From: https://www.spiedigitallibrary.org/journals/Journal-of-Astronomical-Telescopes,-Instruments,-and-Systems on 03 Oct 2023
Terms of Use: https://www.spiedigitallibrary.org/terms-of-use

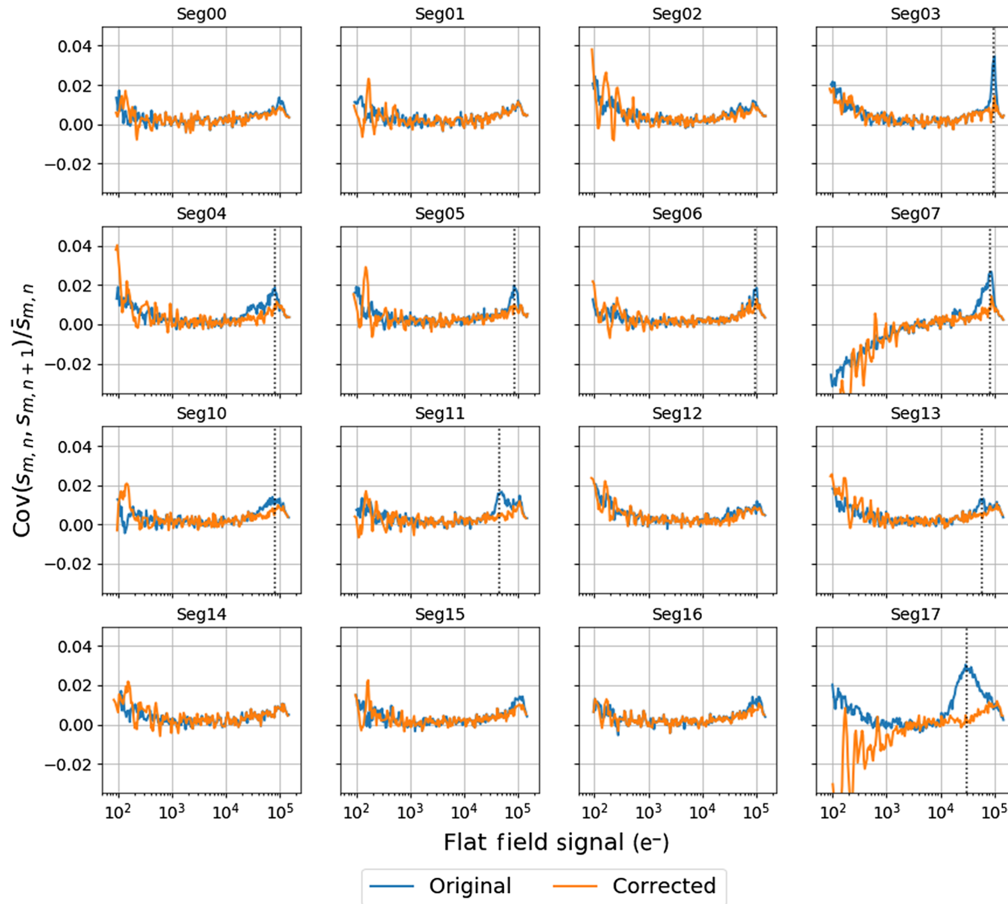

Fig. 18 Normalized serial pixel covariances $\mathrm{cov}(s_{m,n}, s_{m,n+1})/\bar{s}_{m,n}$ for the 16 segments of a single ITL 3800C calculated using all image pixels before (blue) and after deferred charge correction (orange). The vertical dotted lines plotted in a set of subplots indicate per-segment signal levels of interest and are reproduced at the same flat-field signal value across Figs. 3, 5, 7, 12, 14, and 18.

After application of the deferred charge reverse algorithm, the peaked structures in the serial pixel covariances associated with increased deferred charge have been largely reduced to levels consistent with the measurement noise. Based on the shapes of the charge capture functions (Fig. 12), and considering Eq. (3), the order of magnitude of the expected correction to the serial covariances is of 0.01, consistent with the reduction in the sharp peaks. This demonstrating the ability of the correction process to reduce the effect of deferred charge on the serial pixel covariances used for calculation of the brighter-fatter correction kernel. Seg07 and Seg17, however, continue to have large negative pixel covariances at signal levels below 1000 electron that may indicate regimes where there is over correction by the deferred charge reverse algorithm.

8 Future Work and Conclusions

The deferred charge reverse algorithm detailed in this paper has achieved success in reducing the effect of increased serial deferred charge caused by localized charge trapping and the effect of a local, signal-dependent, electronic offset in LSST camera ITL CCDs. Results from corrected flat-field images have shown that the deferred charge correction not only reduces overscan pixel signals to values consistent with only proportional charge-loss from global CTI effects but also removes the associated serial pixel correlations, seen in the covariance measurements, that can increase the error of the brighter-fatter kernel measurement needed for correction of the brighter-fatter effect. The current deferred charge research is focused on two tasks: improving the

Downloaded From: https://www.spiedigitallibrary.org/journals/Journal-of-Astronomical-Telescopes,-Instruments,-and-Systems on 03 Oct 2023
Terms of Use: https://www.spiedigitallibrary.org/terms-of-use

deferred charge reverse algorithm and characterizing the effect of the deferred charge on realistic astronomical source images. These two tasks are complementary; further deferred charge characterization will inform the improvements that may need to be made to the correction algorithm.

The two segments on ITL CCD R02/S02, Seg07 and Seg17, are two examples of segments that still show CTI artifacts caused by deferred charge, even after correction. Both show evidence for remaining degeneracy between the global CTI and localized charge trapping at low signal levels. There are also signal regimes where the reverse algorithm itself introduces residuals in the pixel values, through either overcorrection or undercorrection. Study of these segments and other extreme deferred charge outliers will be important for developing improvements to the deferred charge forward and reverse algorithm that may be needed to more fully capture the behavior of the most extreme cases of deferred charge in a small number of segments of the LSST camera focal plane.

The deferred charge characterization presented in this paper has focused solely on deferred charge effects on flat-field images. Future work will focus on the deferred charge effects on realistically sized source images taken in the laboratory during the partial focal plane testing period of the LSST camera. Serial deferred charge will distort the shapes of source images asymmetrically. These distortions can introduce systematic errors into PSF and galaxy ellipticity measurements. It will also be important to study the derivation of the brighter-fatter kernel from both corrected and uncorrected flat-field images, and the application of the kernel to corrected and uncorrected spot images in order to study the influence of the deferred charge correction on the brighter-fatter correction. This ongoing work will inform the future requirements of the deferred charge correction algorithm in the data reduction pipeline and dictate the extent of improvements that may be necessary in order to maintain the LSST science goals.

Acknowledgments

This material is based upon work supported in part by the National Science Foundation through Cooperative Agreement No. 1258333 managed by the Association of Universities for Research in Astronomy (AURA) and the Department of Energy under Contract No. DE-AC02-76SF00515 with the SLAC National Accelerator Laboratory. Additional Rubin Observatory funding comes from private donations, grants to universities, and in-kind support from LSSTC Institutional Members. This material is based upon work supported in part by the U.S. Department of Energy, Office of Science Graduate Student Research (SCGSR) program. The SCGSR program is administered by the Oak Ridge Institute for Science and Education for the DOE under Contract No. DE-SC0014664. We thank Pierre Antilogus, Pierre Astier, and Claire Juramy for their ongoing work in optimization of the LSST camera CCDs and their related studies of deferred charge in both ITL CCDs and Teledyne e2v CCDs.

References

1. Ž. Ivezić et al., "LSST: from science drivers to reference design and anticipated data products," *Astrophys. J.* **873**, 111 (2019).
2. M. Lopez et al., "Acceptance testing for LSST camera raft tower modules," *Proc. SPIE* **10702**, 107022C (2018).
3. S. Newbry et al., "LSST camera bench for optical testing: design, assembly, and preliminary testing," *Proc. SPIE* **10702**, 1070258 (2018).
4. J. Rhodes et al., "The effects of charge transfer inefficiency (CTI) on galaxy shape measurements," *Publ. Astron. Soc. Pac.* **122**, 439–450 (2010).
5. T. Prodhomme et al., "The impact of CCD radiation damage on GAIA astrometry. I image location estimation in the presence of radiation damage," *Mon. Not. R. Astron. Soc.* **419**(4), 2995–3017 (2012).
6. J. R. Janesick, *Scientific Charge-Coupled Devices*, SPIE Press, Bellingham, Washington (2001).
7. N. C. Hambly et al., "GAIA data release 2," *Astron. Astrophys.* **616**, A15 (2018).

Downloaded From: https://www.spiedigitallibrary.org/journals/Journal-of-Astronomical-Telescopes,-Instruments,-and-Systems on 03 Oct 2023
Terms of Use: https://www.spiedigitallibrary.org/terms-of-use

8. A. Snyder and A. Roodman, "Investigation of deferred charge effects in Large Synoptic Survey Telescope ITL sensors," *J. Astron. Telesc. Instrum. Syst.* **5**(4), 041509 (2019).
9. P. Astier et al., "The shape of the photon transfer curve of CCD sensors," *Astron. Astrophys.* **629**, A36 (2019).
10. P. Antilogus et al., "The brighter-fatter effect and pixel correlations in CCD sensors," *J. Instrum.* **9**, C03048 (2014).
11. W. R. Coulton et al., "Exploring the brighter-fatter effect with the Hyper Suprime-Cam," *Astron. J.* **155**, 258 (2018).
12. C. Lage, A. K. Bradshaw, and J. A. Tyson, "Poisson_CCD: a dedicated simulator for modeling CCDs," https://arxiv.org/abs/1911.09038 (2019).
13. R. Massey et al., "Pixel-based correction for charge transfer inefficiency in the Hubble Space Telescope advanced camera for surveys," *Mon. Not. R. Astron. Soc.* **401**, 371–384 (2010).
14. J. Anderson and L. R. Bedin, "An empirical pixel-based correction for imperfect CTE. I. HST's advanced camera for surveys," *Publ. Astron. Soc. Pac.* **122**, 1035 (2010).
15. J. Skottfelt , D. H. Hall, and B. Dryer et al., "C3TM: CEI CCD charge transfer model for radiation damage analysis and testing," *Proc. SPIE* **10709**, 1070918 (2018).
16. A. Short et al., "An analytical model of radiation-induced charge transfer inefficiency for CCD detectors," *Mon. Not. R. Astron. Soc.* **430**, 3078–3085 (2013).
17. B. T. P. Rowe et al., "GALSIM: the modular galaxy image simulation toolkit," *Astron. Comput.* **10**, 121–150 (2015).
18. N. J. Mostek et al., "Charge trap identification for proton-irradiated p+ channel CCDs," *Proc. SPIE* **7742**, 774216 (2010).
19. J. Skottfelt et al., "Importance of charge capture in interphase regions during readout of charge-coupled devices," *J. Astron. Telesc. Instrum. Syst.* **4**(1), 018005 (2018).
20. R. Massey et al., "An improved model of charge transfer inefficiency and correction algorithm for the Hubble Space Telescope," *Mon. Not. R. Astron. Soc.* **439**, 887–907 (2014).

Adam Snyder received his bachelor of science degree in physics from the University of Illinois at Urbana-Champaign in 2014 and his doctor of philosophy degree in physics from Stanford University in 2020. He is a postdoctoral fellow at the University of California, Davis. His current research interests are studying the impact of satellite mega-constellations on ground-based astronomy, characterization of imaging sensors for precision optical and near-infrared astronomy, and cosmological measurements of dark energy and dark matter. He is a member of SPIE.

Biographies of the other authors are not available.

Downloaded From: https://www.spiedigitallibrary.org/journals/Journal-of-Astronomical-Telescopes,-Instruments,-and-Systems on 03 Oct 2023
Terms of Use: https://www.spiedigitallibrary.org/terms-of-use